SMALL SCALE MECHANICAL BEHAVIOR OF METAL ELECTRODES

A Thesis

by

COLEMAN DILLINGER FINCHER

Submitted to the Office of Graduate and Professional Studies of
Texas A&M University
in partial fulfillment of the requirements for the degree of

MASTER OF SCIENCE

Chair of Committee,	Matt Pharr
Co-Chair of Committee,	George M. Pharr
Committee Member,	Justin Wilkerson
Head of Department,	Andreas Polycarpou

August 2020

Major Subject: Mechanical Engineering

ABSTRACT

Realization of alkali metal anodes would enable batteries with enormous capacities. However, during electrochemical cycling, the deposited metal frequently forms dendrites that can penetrate battery separators, leading to severe safety issues in liquid electrolyte systems. Likewise, in solid-state electrolyte systems, significant issues arise in maintaining adequate interfacial contact between the solid-state electrolyte and the metallic anode during operation. These issues have precluded practical use and are intimately connected to the mechanical behavior of the alkali metals themselves. Still, even the basic mechanical properties of alkali metals remain largely unknown. To this end, this thesis presents a systematic experimental study of the mechanical properties of lithium and sodium metal over multiple length and time scales. Implications of these measurements are discussed in the context of battery science and technology.

ACKNOWLEDGEMENTS

The most important acknowledgement I can give is to Drs. Matt Pharr and George Pharr: you played a foundational role in my growth as a scientist and as a person over the past few years. I am a better person because of you.

Outside of my advisors, I owe thanks to Drs. K. R. Rajagopal, P. S. Hamilton and other faculty who have also played a significant role in my intellectual development and informing my view of academic life.

I've also benefitted from interaction with many insightful students (both undergraduates and graduates) here at Texas A&M, all of whom have pushed me to become a better researcher. I have many students to thank in this regard: Haley Turman, Garrett Hardin, Seunghyun Lee, Omid Zargar, Kamrul Hasan, Wesley Higgens, Yvonne Dieudonné, Chris Walker, Zhiyuan Liang, Russell Rowe, Daniela Ojeda, Temitayo Odunuga, Tim Brown, Nick Barta, and Aashutosh Mistry. Even more notably, I owe my greatest thanks and admiration to Yuwei Zhang. I've had the privilege to work many late hours alongside Yuwei, and his passion and perseverance continue to inspire me.

Finally, I would like to thank my family for their unconditional care and support. I am truly lucky.

CONTRIBUTORS AND FUNDING SOURCES

This work was funded by the support of the National Science Foundation Graduate Research Fellowship under grant No. 1746932.

TABLE OF CONTENTS

PAGE

LIST OF FIGURES

Page

LIST OF TABLES

CHAPTER I

INTRODUCTION[1,2]

1.1 Background related to the mechanical behavior of Li metal

Realization of pure lithium anodes would enable transformative rechargeable battery systems with significantly greater theoretical energy capacities, such as Li-S (2.6 kWh/kg) and Li-Air (3.5 kWh/kg), as compared to current commercial materials such as C-$LiCoO_2$ (0.4 kWh/kg)[1]. Indeed, Li metal is known as the "Holy Grail" of anode materials, as it has the highest theoretical capacity, lowest density, and most negative electrochemical potential of the candidate materials[2]. While a few commercial interests first pursued Li metal batteries nearly 50 years ago, safety concerns preempted its widespread adoption. Early studies found that Li forms dendrites during repeated cycling, leading to short circuits, thermal runaway, and explosion hazards[2]. However, the increasing need for high-energy density power sources has led to a renaissance in Li metal research. Likewise, increased study of both liquid and solid-state electrolytes (SSEs) have paved the way towards safer batteries. However, maintaining reversible Li deposition during cycling has still proven problematic in many battery systems [3-6].

A few studies have shown that the deformation mechanics of the component materials play a key role in the formation/suppression of Li dendrites and the corresponding interfacial stability [7, 8]. The seminal work of Newman and Monroe suggested that the pressure applied to the surface

---

[1] Reprinted with Permission from "Mechanical properties of metallic lithium: from nano to bulk scales" by Cole D. Fincher, Daniela Ojeda, Yuwei Zhang, George M. Pharr, Matt Pharr, 2020. Acta Materialia, Volume 186, 215-222, Copyright 2019 by Acta Materialia Inc.

[2] Reprinted with Permission from "Elastic and Plastic Characteristics of Sodium Metal" by Cole D. Fincher, Yuwei Zhang, George M. Pharr, and Matt Pharr, 2020. Applied Energy Materials, Volume 3, 1759-1767, Copyright 2020 by American Chemical Society.

of the anode via the separator directly affects the propensity for dendrite formation[9]. Recently, the results of Jana and Garcia indicate that dendrite morphology and growth are a direct product of the competition between the rate of Li deposition and the rate of Li's plastic deformation under pressure[10]. Implicitly, Jana and Garcia's findings may suggest that the morphology of lithium possesses a strong dependency on charging rate and feature size. Meanwhile, experimental studies by Gireaud et al.[11], Wilkinson et al.[12], and Hirai et al.[13] attest to the effects of pressure on the Li deposition morphology, and studies by Dollé et al.[14], Brissot et al.[15], and others demonstrate that a strong rate-dependency of Li deposition morphology exists across multiple length scales[16]. Beyond the growth of dendrites in liquid electrolyte systems, multiple studies outline the importance of deformation mechanics in maintaining stable interfacial contact between the SSE and the anode in all-solid-state batteries (ASSB's)[2-4, 6, 17-20]. For instance, Li et al. observed improved battery performance with increased interfacial contact under mechanical loading for an ASSB[5]. Taken together, these studies suggest the potential to harness mechanics for realizing more stable Li electrodeposition.

While a few recent studies have measured some of the mechanical properties of Li, the community still lacks a holistic multi-length and time scale portrait. Three individual studies of lithium metal under compression at the nano-[21], micro-[22], and bulk[23] scales suggest that the yield strength of Li varies by significantly more than an order of magnitude. Additionally, studies of lithium metal in tension by Tariq et al.[24], followed very recently by Masias et al.[25] and LePage et al.[26], indicate highly ductile and strain-rate dependent plasticity in bulk lithium. However, directly comparing these results proves problematic, given the studies' various methods of sample preparation and loading conditions (e.g., geometries and rates). For instance, recent

work by Campbell et al. suggests that cold-working of lithium metal can alter its hardness by nearly an order of magnitude [27]. In addition, relating mechanical measurements for Li metal to the mechanical properties of Li electrodeposits requires careful consideration of the plastic volumes deforming during mechanical testing, which are typically much smaller in nanoindentation than in bulk tensile testing. Given these potentially confounding factors, reliably representing the deformation mechanics of Li dendrites requires a comprehensive study of lithium metal as commercially prepared for practical battery applications and over the relevant length and time scales.

To this end, chapter II of this thesis provides a mechanical study of the most commonly used form of Li metal in the battery community: high-purity Li metal foil. Through a combination of bulk tensile testing, nanoindentation, and finite element analysis, we systematically characterize the mechanical properties of Li metal across length scales, nano to bulk, and time scales, by varying the loading rates over a significant range. We also detail the implications of these measurements in terms of the performance of Li metal anodes.

1.2 Background related to the mechanical behavior of Na metal

Sodium-based batteries have garnered recent attention largely due to Na's abundance, low cost, and limited geographic constraints[28, 29]. As such, they may find applications where Li-based batteries are not as viable, such as in grid-scale energy storage from renewable resources[30]. Additionally, unlike Li, Na's inability to alloy with Al enables pairing Na metal anodes with Al current collectors, as compared to the heavier and commonly-used Cu current collectors, thereby simplifying the manufacturing process and reducing manufacturing costs by an

estimated 8%[31, 32]. Of potential candidates for anodes in sodium-ion systems, sodium metal itself has the lowest electrochemical potential (-2.71 V vs. the standard hydrogen electrode) and the highest theoretical capacity (1165 mAh/g)[28, 29]. However, growth of Na dendrites can produce short-circuits and induce explosion hazards[28, 33, 34]. In fact, a recent study suggests that Na metal electrodes are even more prone to dendritic growth than are those of Li[35]. Additionally, reduction of most electrolytes occurs readily at Na's surface, producing a solid electrolyte interphase (SEI), which consumes active material[28, 36, 37]. Finally, Na metals suffers from so-called "infinite volume change" due to its host-less nature (i.e., it involves a plating process)[33]. Cycling exacerbates degradation, ultimately resulting in capacity fading and safety hazards that must be addressed prior to practical implementation[36, 38, 39].

The mechanical properties of the Na metal anode play a key role in the cycleability of the battery[3, 12, 13, 40]. For metallic anodes in liquid electrolyte systems, mechanical pulverization and capacity loss remains a significant challenge, largely due to dendritic/non-uniform growth during electrochemical deposition[41]. Likewise, loss of contact during cycling at the interface between a solid-state-electrolyte (SSE) and the metallic electrode continues to stymie development of solid-state-batteries[17, 19, 42-44]. For such systems, the mechanical properties (i.e., yield stress, elastic modulus, and time-dependent plasticity) dictate the stress sustained by the electrode (and the surrounding electrolyte) under various geometries and loading conditions, e.g., at different charging rates. The stresses in turn may affect the electrode kinetics (by modifying the total electrochemical potential of the electrode)[45-48], the growth morphology under cycling[9, 45], and/or the integrity of the contact at the anode/SSE interface[18, 49, 50]. Progress regarding solid-state Na batteries appears encouraging[42, 51-53]. However, the recent study by Spencer Jolly et

al. indicates that creep of Na is a crucial process in overcoming void formation at the SSE/anode interface, thereby averting cell death[50]. Strategies to mitigate these cycling issues will require a thorough understanding of Na's mechanical properties.

Despite the importance of Na's mechanical properties, surprisingly little is known. A few studies[54-58] have presented single crystal elastic constants of Na at a variety of temperatures (see Table 1). However, no studies have probed the elastic properties of aggregate (polycrystalline) sodium metal. Even more pressing is the lack of knowledge of Na's plastic properties. More than a century ago, Edwards investigated the resistance of bulk Na using Brinell style tests, reporting a hardness number of 0.07[59]. However, these samples were likely contaminated due to air exposure during testing. In addition, Herke, Kirchner, and Schoeck present stress-strain curves of Na in tension at various temperatures, but no strain-rate is explicitly stated[60]. Furthermore, the plot units are not clearly defined, but the trend presented appears to show that the critical resolved shear stress was approximately constant between 200 - 300 K[60]. Lastly, Sargent and Ashby[61] conduct creep tests at room temperature, but do not present other important mechanical information (such as stress-strain curves).

Given this relative dearth of information, we detail mechanical properties of sodium metal at room temperature in chapter III of this thesis. Through nanoindentation, we quantify elastic properties of Na metal. By combining nanoindentation with microhardness testing and bulk compression tests, we characterize Na's plastic response across multiple length and time scales. We compare the mechanical characteristics of Na with those of other candidate metallic anodes of rechargeable batteries. Finally, we discuss practical implications of this work, with an eye toward battery scientists and designers.

CHAPTER II

MECHANICAL BEHAVIOR OF LITHIUM METAL[3]

2.1 Methods

2.1.1 Li Sample Preparation for Nanoindentation

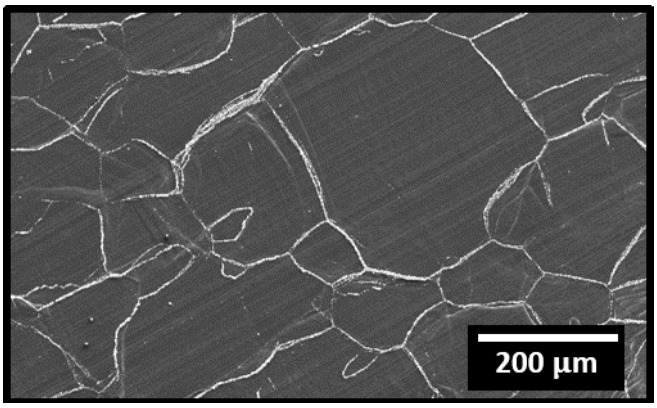

Figure 1. A scanning electron micrograph of Li foil prior to surface preparation. The grain size is near 110±20 μm (average ± standard deviation) using the linear intercept technique.

As-received lithium foil, as seen in Figure 1, possesses significant surface roughness and occasionally chemical contamination. Thus, the indentation samples required careful preparation prior to testing. All sample preparation and indentation occurred within an argon-filled glovebox with less than 0.1 ppm O_2 and H_2O. The lithium foil (Sigma Aldrich, 99.9% purity on trace metal basis) was first sectioned into an 8 mm by 8 mm square and adhered to a nanoindentation mount at 70°C using Crystal Bond 555 adhesive. The surface of the foil was prepared by shaving it with a razor blade to reveal fresh lithium with minimal surface contamination. The sample and

[3] Reprinted with Permission from "Mechanical properties of metallic lithium: from nano to bulk scales" by Cole D. Fincher, Daniela Ojeda, Yuwei Zhang, George M. Pharr, Matt Pharr, 2020. Acta Materialia, Volume 186, 215-222, Copyright 2019 by Acta Materialia Inc.

indentation mount was placed between two well-oiled borosilicate glass plates (1/4-inch-thick, lubricated with Sonneborn PD-28 highly refined white mineral oil), and the plates were placed inside a hydraulic crimper and pressed until the Li was flat. The sample and indentation mount were immediately removed and mounted on the nanoindenter, also located within the glovebox. An optical micrograph of an indentation made in this way is shown in Figure S1. By conducting experiments on an as fabricated sample before and after a 24 hour anneal at 0.8 * $T_{m,}$ we assessed potential of surface damage due to sample preparation. Full details can be found in the supplementary information section titled "Assessing the possibility of surface damage during sample preparation." In summary, however, we find minimal changes in hardness after annealing at 0.8*T_m, which implies that the sample preparation is unlikely to affect the hardness measurements presented in this study.

2.1.2 Nanoindentation Methods

Nanoindentation measurements of hardness, *H*, and elastic modulus, *E*, were made using a Nanomechanics Nanoflip indentation system operated in the glove box. All measurements were performed with a Berkovich triangular pyramid indenter using the continuous stiffness measurement technique (CSM)[62, 63].

Continuous stiffness measurements of mechanical properties require precise knowledge of the indenter area function, which is normally determined in tests of a fused silica calibration standard [62, 63]. However, in this study, an area function was required to much larger depths than can be achieved in fused silica. As such, the fused silica area function was supplemented by calibration measurements from polycarbonate (Makrolon®, 0.08 inch thickness, ASTM D3935 class 1 polycarbonate sheet) in a manner similar to that described by Ginder and Pharr[64]. This

area function was calibrated over the range of 250 nm to 10 μm; thus, E and H measurements outside of this range are discarded.

Lithium has an extremely high modulus-to-hardness ratio *E/H* (in the range 500-1000), and consequently, very little elastic recovery occurs during unloading; in fact, the depth recovery is less than 1% of the total penetration depth, *h*. Using this observation, the total depth of penetration can conveniently be used as a good measure of the contact depth, h_c, (therefore rendering the sink-in correction to contact depth unnecessary), provided that one important correction is made. Specifically, lithium is a material that exhibits pile-up during indentation, which is not properly accounted for in standard nanoindentation data analysis procedures. To include pile-up effects here, several large indentations were optically imaged under oil and measured to determine the contact area. Based on the known area function, these measurements indicated that due to pile-up, the contact depth is 11% greater than the measured indenter penetration depth, that is, $h_c/h = 1.11$. Thus, the depth used in evaluating the contact area A_c was taken as 1.11 times the measured indenter penetration depth. The hardness then followed from $H = P/A_c$, where P is the instantaneous indentation load. We should note that the degree of pile up depends significantly upon the E/H ratio of a material, and thus accuracy of the pile-up assumption (that $h_c/h = 1.11$) may vary with depth for a material with depth-dependent hardness[62].

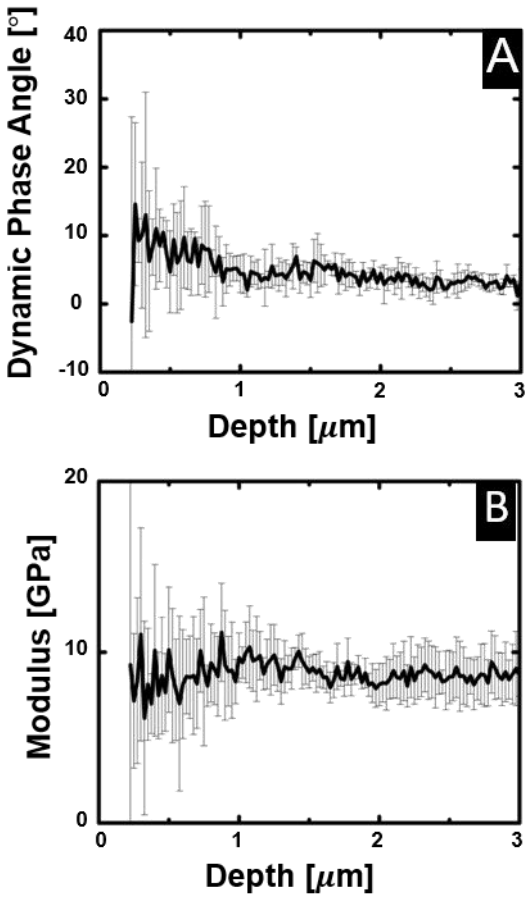

Figure 2. Nanoindentation tests, with the curves representing the average of five indents and the error bar representing the standard deviation of the set of indents. Displayed tests were conducted with a constant $\dot{\boldsymbol{P}} = \mathbf{12.5}\frac{\mu N}{s}$ to a depth of 3 μm. A) the dynamic phase angle suggesting negligible plasticity error, B) the elastic modulus. Individual tests can be seen in Figure S2.

An important factor in accurately measuring the modulus of lithium by nanoindentation CSM methods is what has recently been identified Merle et al. as "plasticity error" [26]. This systematic error originates from a breakdown in the assumption that deformation during the small force oscillation used to make CSM measurements is entirely elastic, that is, there is no plastic deformation induced by the oscillation. Plasticity error becomes significant in materials with

higher *E/H* ratios, like lithium. Fortunately, it has also been found that if the phase shift between the force and displacement oscillations as measured by the lock-in amplifier used to make the CSM measurement is less than 10°, then plasticity error is negligible [26,27]. Indeed, the measurements in Fig. 2 meet this 10° criteria, allowing for the use of continuous stiffness to collect the contact stiffness and ultimately measure the elastic modulus.

It is notable that the measurements in Fig. 2B based on the Oliver-Pharr approach (using the measured dynamic stiffness and depths between 0.25 and 3 μm) yield an elastic modulus of 9.43 ± 0.5 GPa that is independent of depth. Since this modulus is consistent with previous studies, the data suggest that the measurements at the depths reported here are not influenced in any significant way by an oxide/nitride/hydroxide or other contaminant layer on the surface.

2.1.3 Tensile Testing

A custom-built tensile tester was configured within the glovebox for the purpose of performing tests in a controlled environment most suitable for the air-sensitive lithium without having to transfer the specimens. The apparatus (seen in Figure S3) consisted of a LC703-200 load cell (Omega Engineering) in conjunction with an INF-USB2 model data acquisition system (Interface Inc.), and a ClearPath-MCPV model integrated servo motor system (Teknic) assembled onto an FGS-250W test stand (SHIMPO). The load cell calibration was validated against an Instron 5943 benchtop tensile tester with a 1 kN load cell (Figure S4). To further ensure the system's accuracy, standard high density polyethylene (HDPE) tensile specimens were tested both with the in-glovebox tensile tester and with the benchtop tensile tester (Instron 5943) at strain rates of 5E-1 s^{-1} and 5E-4 s^{-1} (Figure S5), with 100 Hz and 10 Hz acquisition rates, respectively. For the lithium data, we also implemented a toe compensation to mitigate the effects of system slack[65].

Additionally, a machine compliance determination (effects of which are seen in Figure S6), was conducted in accordance with the procedure outlined by Kalidindi, Abusafieh and El-Danaf [66], taking the elastic modulus of lithium as 9.4 GPa as determined in this study (from Figure 2B). Lithium metal ribbon (Sigma Aldrich, 99.9% purity on trace metal basis), 45 mm wide and 0.75 mm thick, was stored in an argon-filled glovebox with less than 0.1 ppm O_2 and H_2O. A dogbone-shaped die (gauge width of 10 mm and length of 55 mm, 5 mm fillet radius, and total length of 105 mm) was used to stamp out the test specimens from the as-received lithium ribbon. Using the die ensured geometric uniformity among samples.

Load data during tensile testing was collected at 100 Hz for nominal strain rates of 5E-1 s^{-1}, 5E-2 s^{-1}, and 5E-3 s^{-1} and at 10 Hz for 5E-4 s^{-1} tests. For the 5E-4 s^{-1} tests, a 5-term Fourier smoothing fit was applied to the data at strains of 0.002 and larger. The strains reported are the nominal (engineering) strains. The displacements measured by the tensile tester were verified to match experimental data during preliminary testing by use of a digital length scale and digital image correlation.

2.1.4 Finite Element Analysis

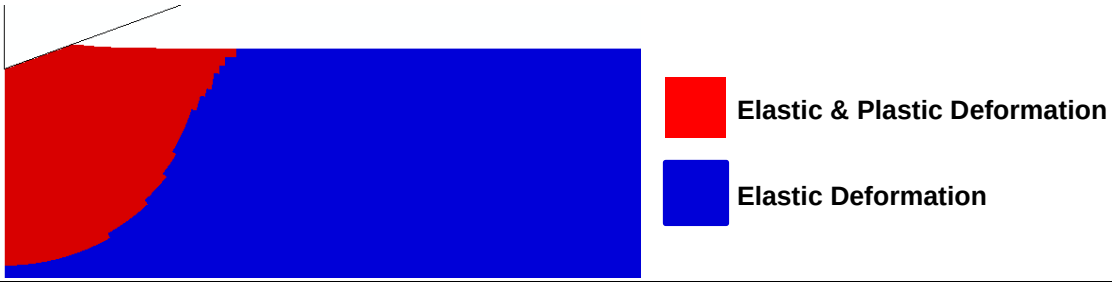

Figure 3. The actively yielding elements (AC_Yield output) from ABAQUS used to estimate the volume of the plastic zone under the indenter during nanoindentation experiments. The red elements represent the elements undergoing plastic deformation, while the blue elements undergo elastic deformation only.

Finite element simulations of the indentation process were conducted to estimate the size of the plastic zones for an analysis of length scale effects on strength. The axisymmetric elastic-plastic simulations (Figure 3) consisted of rigid indenter with an internal angle of 70.3° (the cone angle which possesses the same self-similar contact area with respect to depth as a Berkovich indenter tip) in contact with a solid mesh of CAX4R elements. Nonlinear geometric effects were included. The elastic behavior of the solid was assumed to be isotropic with an elastic modulus of 9.4 GPa and a Poisson's ratio of 0.3. The behavior of the solid was prescribed as elastic-plastic, with the plastic flow stress defined as a function of plastic strain by inputting stress-strain data from an experimentally measured lithium stress-strain curve collected at 5E-2 s^{-1} strain rate, using a 0.002 strain offset. The "indenter" was specified to have x displacement, z displacement, and all rotations fixed at zero (U1=U3=UR2=UR3=UR1=0) with a displacement downwards by the contact depth (a distance of U2= -h_c). The bottom surface of the solid was given a fixed boundary condition, while the left side was given a y-axis symmetric boundary condition. A finite-sliding interaction was defined between the indenter and substrate surface, using surface-to-surface discretization and adjustment only to remove overclosure. This interaction was defined to have frictionless tangential behavior. The simulations produced a plastic volume which, if treated as a hemisphere, has a radius of $11.5 * h_c$.

2.2 Results

The red and black curves in Figure 4A show the hardness as a function of indenter penetration depth from nanoindentation tests conducted at two different values of $\dot{P}/P$, 0.5 and 0.05 s^{-1}. Each curve is the average of 7 individual tests, with error bars representing one standard deviation. The data is plotted for depths of 0.25 μm (the lower bound for area function calibration)

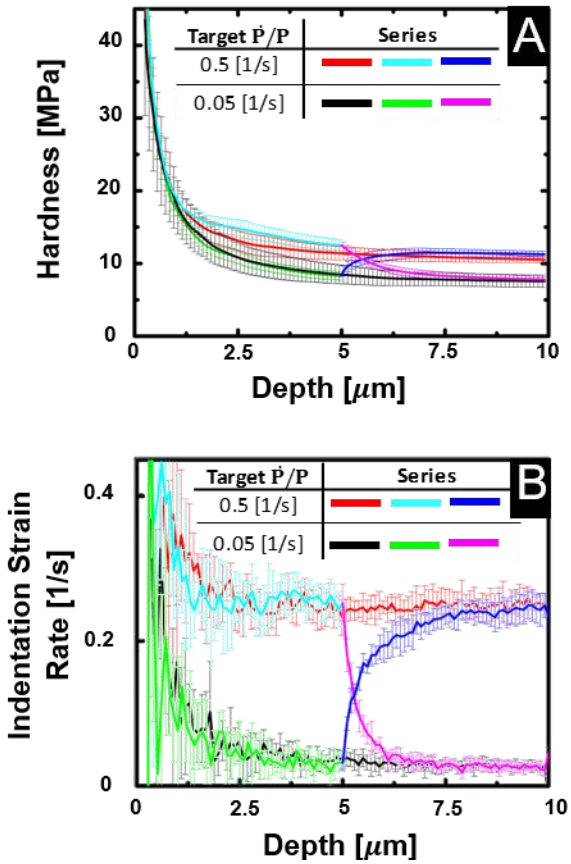

Figure 4. Nanoindentation tests, with each displayed series representing the average of 7 individual indents conducted under identical test conditions: A) indentation hardness, and B) the measured indentation strain rate. Scatter bars span one standard deviation from the mean. The original nanoindentation data and load depth curves can be found in the supporting information.

and higher. Plots of the individual indentation load-depth curves, as well as the individual strain rates versus depth, and hardness versus depth can be found in Figures S7-S10.

Nanoindentation tests are often conducted at constant $\dot{P}/P$ because this condition produces a constant indentation strain rate, $\dot{h}/h$, if the hardness does not vary with depth. However, for the data in Fig. 4A, it is clear that the hardness at smaller depths decreases rapidly before approaching a relatively constant value at larger depths. As a consequence, the depth dependence of the indentation stain rates shown in Fig. 4B also shows a decrease before achieving a relatively

constant value. The decrease in hardness at the beginning of the test thus suggests that there is a significant indentation size effect, although some of the decrease may be due to strain rate effects. In addition, we cannot completely rule out the possibility of influences from a hard surface film due to contamination by, for example, oxygen and/or nitrogen. However, if a hard surface film exists, it must be very thin since the elastic modulus data in Figure 2B show no indication of a different surface layer. Because the hardness appears approximately constant with indentation depth at depths near 10 μm, we fit the hardness and corresponding indentation strain rate to establish the stress exponent for steady state flow ($\frac{\dot{h}}{h} = A * H^n$), which gives a stress exponent of n=6.9. Figure 4 also includes data from two tests in which $\dot{P}/P$ and the corresponding indentation strain rate was abruptly changed by an order of magnitude at an indentation depth of 5 μm. The curve that transitions from cyan to magenta is for a rate decrease from $\dot{P}/P$ = 0.5 s^{-1} to 0.05 s^{-1}, while the curve that changes from green to blue is for a rate increase from $\dot{P}/P$ = 0.05 s^{-1} to 0.5 s^{-1}. The data from these tests indicate that after a brief transient, the hardness and indentation strain rate both recover to the values observed in the tests in which $\dot{P}/P$ was held constant during the entire test, thus indicating a strong strain rate dependence of the hardness, and one that is essentially independent of the loading history. Collectively, the nanoindentation results in Fig. 4 demonstrate that lithium exhibits both size and strain rate dependent hardness (i.e., strength).

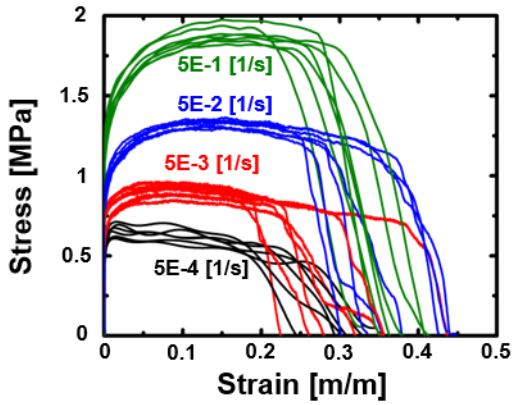

Figure 5. Stress-strain relationship from uniaxial tension testing of as-received bulk lithium metal, acquired at nominally

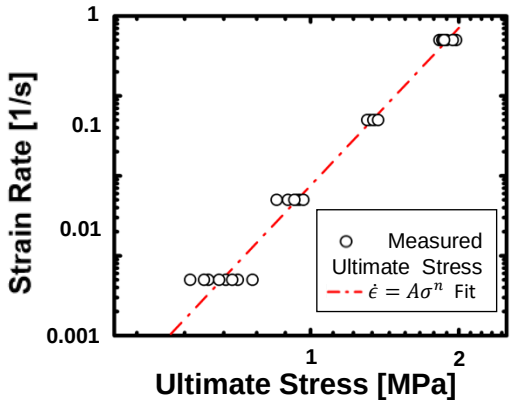

Figure 6. Strain rate versus ultimate stress from tensile testing results. The trend line represents the curve $\dot{\epsilon} = A\sigma^n$, where A=0.0708 $[1/(\mathrm{MPa}^{\mathrm{n}} * \mathrm{s})]$ and $\mathrm{n} = 6.55$.

Figure 5 shows results from tensile tests of bulk Li metal. Taking the yield stress as the engineering stress at 0.002 strain, the average yield stresses at strain rates of 5E-1 s^{-1}, 5E-2 s^{-1}, 5E-3 s^{-1} and 5E-4 s^{-1} are 1.26±0.05, 0.89±0.05, 0.71±0.08, and 0.57± 0.04 MPa, respectively. Thus, a strong strain rate dependence of the strength is also observed in the tensile tests. Furthermore, the average failure strain does not appear to strongly depend on strain rate and has an average value around 0.35. This is considerably greater than the 0.03 to 0.08 ductilities reported by Tariq et al.[24].

Because the stress-strain curves rise to a near-constant or steady state flow stress, one can use the data obtained in the tensile tests to establish the stress exponent, *n*, for steady state flow (or creep). To do so, the strain rate dependence of the ultimate stresses (maximum stress measured during the test) in Figure 5 have been plotted in Figure 6. The data appear quite linear, suggesting a stress exponent n = 6.55, a value in a range that is often indicative of time-dependent plastic deformation controlled by dislocation climb. This value is well within the normal range of

approximately 1-7 for most pure metals and alloys[67]. Furthermore, this value appears comparable to the stress exponent as determined for nanoindentation (n=6.9). The stress values determined in this study also match well with recent works of LePage et al.[26] and Masias et al.[25], who note that dislocation climb is likely the dominant deformation mechanism for their observed stress exponents of 6.6 and 6.56, respectively.

2.3 Discussion

2.3.1 The Mechanical Properties of Li Metal

The data obtained in this study along with that of several previous investigations provides a means by which the strength and plastic flow behavior of lithium can be assessed over a wide range of length and strain rate scales. To do this, data for length scale influences on yield strength from several investigations are plotted in Fig. 7, and data for the strain rate dependencies in Fig. 8. The plots include data from hardness, tension, and compression tests. To facilitate comparison, data from hardness tests have been converted to yield strengths, σ_y, assuming that the Tabor relation is approximately correct, that is, $\sigma_y \cong H/3$. With the aforementioned goal of comparing the tested length scale to a feature size of relevance in the context of a Li metal deposit, we first establish an appropriate length scale for each test. For micropillar and bulk tensile/compression testing, the authors take the square root of the specimen cross sectional area. For indentation testing, the authors use the cube root of the plastic zone size (~11.5*h_c), as determined herein through finite element analysis. The grain size of our specimens (Figure 1) is 110 ± 20 μm (average $\pm$ standard deviation) using the linear intercept technique, based upon the analysis of the area of

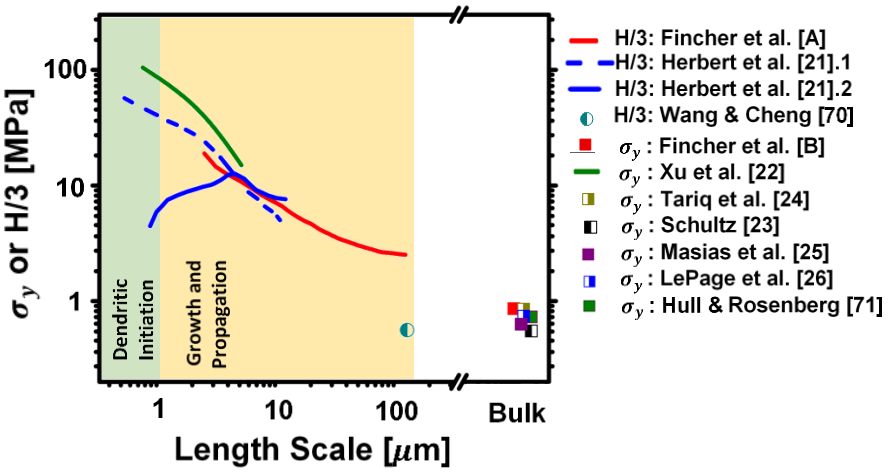

Figure 7. The σ_y or H/3 is plotted versus a representative length scale, displaying data from this study as well as previous literature. For this study, the yield stress from bulk tensile testing was taken as the flow stress at 10% strain. Feature sizes corresponding to dendritic initiation are shown as a green background, while the yellow region corresponds to dendritic growth and propagation.

350 grains. As such, the plastic zone size is smaller than the grain size at small nanoindentation depths but approaches the grain size at large nanoindentation depths. Data from tension and compression tests are plotted directly as the measured flow strength at 0.1 strain assuming that there is no tension/compression asymmetry, as justified based on the study of Gorgas et al., who found only a minor asymmetry (<10%) between the stress in tension and in compression of Li at room temperature [68]. We note that many of the tests presented in Figure 7 were performed at different strain rates, thereby potentially conflating effects. However, Figure 8 shows that the flow stress of Li varies by less than a factor of 10 over strain rates varying by a factor of $>10^6$ from various bulk tests. Thus, the strain rate influences on the data in Figure 7 are probably less significant than are the size effects.

The strengths measured in this study are plotted in Figure 7 as a red line [A] for the nanoindentation tests (at $\dot{P}/P$=0.05 [1/s]) and as the red square symbol for the bulk yield strength

measured in the tensile tests [B]. The value plotted for yield strength in Figure 7 (symbol [B]) is the average yield strength measured across the strain rates 5E-4 s^{-1} to 5E-1 s^{-1}, as presented in Figure 8. The measured H/3 values from nanoindentation decreases precipitously from an initial value near 14 MPa at a representative length scale of ~2.3 μm to nearly 6.7 MPa at a length scale of ~10 μm, and finally 2.5 MPa as the length scale approaches ~115 μm. While the H/3 value from nanoindentation at large depths (2.5 MPa) does not converge to the 0.86 MPa average yield strength measured from bulk testing, some offset between the two quantities may be expected due to factors such as the difference in effective strain rate in the indentation versus the tensile test.

Herbert et al.[21] conducted nanoindentation on lithium thin films deposited using thermal evaporation. For these measurements, denoted [21].1 in Fig. 7 and shown as a dashed blue line, a constant loading rate of 12.5 μN/s was used on an 18 μm thick film, yielding H/3 values that decrease from approximately 60 to 5 MPa as the length scale increases from 0.5 to 10.5 μm. Other nanoindentation results from Herbert et al. were obtained using constant $\dot{P}/P$ experiments on a 5 μm thick film, plotted in Fig. 7 as the solid blue line [21].2. Here, the hardness initially increases until reaching a maximum and subsequently decreases at a length scale of ~4 μm. Herbert et al. argue that this behavior results from a transition from diffusion to dislocation-mediated flow [69]. After the maximum, the data from this study appear to be in fairly good agreement with the results obtained here, that is, displaying similar values of H/3 as the length scale approaches 10 μm.

The micropillar compression results obtained by Xu et al.[22] as plotted as the green line in Figure 8 also display significant size-dependent strength, with size in the case being the pillar diameter. It should be noted that size-effects may manifest differently in micropillar experiments than in indentation due to differences in the loading and specimen geometry. Furthermore, the

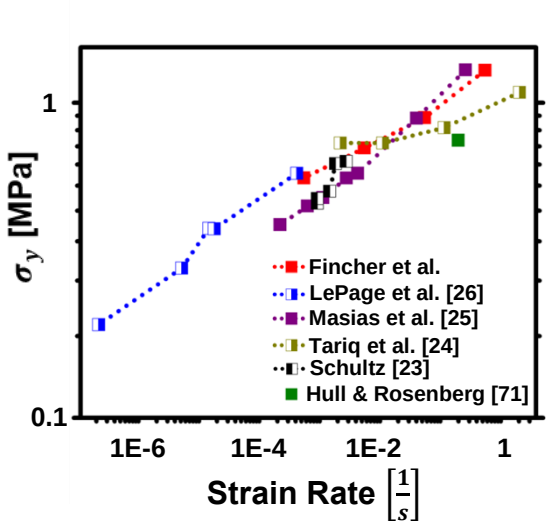

Figure 8. The yield stress $\boldsymbol{\sigma_y}$ plotted versus strain rate for bulk tests in this study and in previous literature.

lithium used for Xu's study was melted and recrystallized, perhaps possessing significantly larger grains than in as-received lithium. As a result, Xu et al. suggest that their measurements represent single crystal compression, and the corresponding critical resolved shear stress values vary between ~5 and 30 MPa for pillars between 1 μm and 10 μm at a 5E-3 s^{-1} strain rate in their work. Assuming that oxidation exposure and contamination from the gallium focused-ion-beam (or air during transfer) did not affect their results, they observe comparatively higher yield strengths but with generally the same downward trend with length scale observed in this study.

Wang and Cheng [70] combined nanoindentation load-depth curves with an iterative finite element model to report a yield stress of 0.56 MPa under static deformation in as-received lithium metal foil. This data appears on the same order of magnitude as that reported here but slightly lower than others in literature, which may be attributable to a variety of factors such as the uncertainty in indentation strain rate or possible scatter in the data.

A few studies of lithium in bulk polycrystalline form are included in Figures 7 and 8. Schultz [23] conducted compression testing in atmosphere (air) on 1-11/16" diameter, 1" long cylinders of 98% purity lithium and measured the yield strength in compression as 0.55 MPa at strain rates between 0.08- 0.25 s^{-1}. In a separate study, Tariq et al.[24] measured an average yield stress of 0.85 MPa in tension tests at strain rates between 0.002 – 1.05 s^{-1} using specimens of unspecified size. Their samples exhibited rapid work hardening and failed at or before a strain of 0.08 [m/m]. Masias et al. [25] tested cylindrical specimens of bulk Li in tension and compression, finding a flow stress of 0.74 MPa at a strain rate of 1E-3 s^{-1}. They also observed significantly different behavior between tension and compression, noting that "frictional forces likely played a role in affecting the stress-strain behavior" for their measurements in compression. LePage et al.[26] tested Li foil in tension, finding a flow stress of 0.63 MPa at a strain rate near 3E-4 s^{-1}. Hull and Rosenberg[71] tested bulk samples of Li in tension, finding a yield stress of 0.73 MPa at a strain rate of 1.8E-3 s^{-1}. However, these authors noted the existence of an oxide film on the specimen, calling into question the role of contamination in their results.

Overall, the bulk testing results in Figures 7 and 8 seems to indicate that the yield stress of bulk Li metal resides between 0.5 and 1 MPa, depending on the strain rate. Meanwhile, the nanoindentation and pillar compression data indicate that the feature size may play a significant role in Li's response at length scales less than 100 μm.

Going forward, pin-pointing the influence of structure on the mechanical properties of Li metal remains an important task. Of the listed studies in Figure 7 and 8, only LePage et al.[26] gives the grain size explicitly, with the stated value being 150 μm, similar to the 110 μm measured in this study. While no grain size is stated explicitly in [69], Herbert et al. does show that the grain

boundaries can play a significant role in the deformation of Li, based on the applied load required to cause a transition in plastic flow behavior of highly pure Li. However, the grain size and purity of Li metal commonly electrodeposited during battery operation remains unclear.

2.3.2 Implications for Li Metal in Battery Applications

The size and rate dependency of the yield strength presented in this work likely play a key role in the morphology and reversibility of electrodeposition during electrochemical cycling of Li metal anodes. Analyses have suggested that lithium dendrites initiate with tip radii ranging between 0.1 and 1.5 μm (shown in the green region of Figure 7) [72-79]. Moreover, electrodeposits have been observed in experiments as having various sizes on the micron scale depending on charging conditions during their formation[10, 80-83] (shown in the yellow region of Figure 7). Likewise, several experiments have already shown an important relationship between the stress applied to electrode stacks by mechanical pressure and the resulting dendrite morphology. In particular, when constrained in a coin-cell geometry, increasing stack pressure has been shown to produce more blunt electrodeposits [11, 12]; these flatter electrodeposits benefit from increased uniformity of local current density, leading to increased cycle life[84]. The yield stress (or equivalently, H/3, in hardness testing) represents a maximum stress level of stress that can be imposed on Li electrodeposits prior to permanent deformation (i.e., flattening). As such, the results presented here serve as a basis to estimate the pressure required to blunt electrodeposits of various sizes with the goal of improving performance.

The relevance of deformation mechanics to many other physical processes in lithium metal batteries with liquid electrolytes remains a topic of debate. A recent study by Wang et al. showed that a significant degree of stress accompanies the deposition process itself, even in the absence of

an applied stack pressure[85]. Since the chemical potential of a species depends on the applied stress[86, 87], the extent to which the local stress modifies the chemical driving forces and plays a role in the homogeneity of electrodeposits warrants further investigation. Beyond reversibility of electrodeposition, so called ‘dead Li’ remains a significant challenge for the battery community[16, 88, 89]. Specifically, lithium can detach or fracture from the electrode during cycling, leading to loss of active material and capacity fade. Again, the exact extent to which dead Li formation depends on deformation mechanics is an open topic. Furthermore, while various studies have outlined the relationship between charging rate and dendrite morphology [14, 15], more analysis is warranted regarding the extent to which Li’s strain-rate dependent strength influences this relationship.

Overall, the results presented herein suggest that work focused on 3D current collectors[90, 91], seeding deposition of Li[92], or otherwise tuning the electrodeposit morphology and feature sizes could prove beneficial for achieving stable and reversible Li deposition in liquid electrolyte systems.

Future work should consider focusing on structure-property relationships in lithium, given the influence of microstructure on both its intrinsic underlying mechanics and the electrodeposition process. Indeed, two recent studies of dendritic Li [93] and Mg [94, 95] have shown that dendrites possess significantly different mechanical properties (modulus and hardness) as compared to the bulk material. Whether this alteration occurs due to impurities or from a change in the physical structure of the material (i.e., porosity or crystalline texture) remains an important question. Thus, future studies should seek to understand the influences of impurities, either those present in Li initially or those introduced during cycling, on the mechanical and transport behavior

of Li. The grain structure of Li may also play a significant role in the stability of Li metal electrodes. In fact, one previous study has found that grain size of Li can affect the battery's coulombic efficiency[96], while another study showed that a coupling exists between grain texture and electrodeposit morphology[97]. In electroplated systems, grain boundaries increase the local density of activation sites[98]. As a result, the grain boundaries likely act as a "point effect of diffusion," a small disturbance to the local diffusion of ions which could lead to local stress intensifications, as discussed in the recent work of Herbert et al.[99] Additionally, in other metals, grain boundaries have been shown to promote the local formation of passivating films[100]. Thus, ample work remains in understanding the interplay between Li metal's structural evolution and ultimate performance in batteries.

Further chemo-mechanical study also remains in understanding the stability of Li metal deposits. As a BCC metal with a melting temperature of 180.5°C[101], Li's temperature-dependent mechanical properties likely modify the conditions required to maintain a mechanically stable electrode across a range of temperatures. While the work herein studied Li metal at room temperature ($\approx$0.65 T_m), the works of LePage et al.[26] as well as of Hull and Rosenberg[71] characterize the temperature dependence of Li's properties across a range of temperatures, where LePage et al. show that the flow stress varies by nearly a factor of three between -75°C and 125°C[26]. Meanwhile, Love et al.[102] show that even the general dendrite morphology changes for different temperatures of practical relevance in a liquid electrolyte system. However, further work studying the coupling of temperature and mechanics in both solid and liquid electrolyte systems would elucidate this important issue further. Additionally, the rate-dependence of

plasticity likely plays a key physical role in maintaining stable electrodeposition. While Ferrese and Newman[45] did provide some insight into the effects of plasticity on the stability of Li metal, their work neglected any rate dependency of the plasticity. Jana and Garcia[10] recently showed the effect of rate-dependent plasticity in determining whether a protrusion tends to elongate or flatten under a variety of conditions. However, further chemo-mechanical modelling which incorporates rate-dependent plasticity could provide detailed estimations of the interfacial stresses present in solid-state batteries.

CHAPTER III

MECHANICAL BEHAVIOR OF SODIUM METAL[4]

3.1 Methods

3.1.1 Sample Preparation

The condition of as-received sodium metal (Sigma Aldrich, 99.9% purity cubes) poses challenges to indentation and tensile testing due to both the initial geometry (a cube with ~1 cm edge length) and because the surface is often covered with a thin purple film layer. In an attempt to mitigate effects of sample contamination, all samples were prepared in an argon glovebox possessing less than 0.1 ppm O_2 and H_2O. Oil (Sonneborn PD-28 highly refined white mineral oil) used for sample preparation was stored in the glovebox with 3Å molecular sieve to remove moisture inside the container for more than 1 month prior to use[103]. The as-received grain size appeared to be near 450 ± 220 μm based upon the linear intercept technique.

For indentation testing, the sodium cube was sectioned using a new razor blade to reveal a shiny and pristine surface. Mineral oil was immediately applied to the exposed surface after sectioning. The backside of the sample was then adhered to a nanoindentation mount using Loctite gel adhesive. The mounted sample was placed between two well-oiled borosilicate glass plates. These plates were placed inside a hydraulic crimper and pressed to flatten the sample. The sample and indentation mount were immediately removed and mounted on the nanoindenter (also within the glovebox). All data within this study was collected within three hours of sample preparation.

---

[4] Reprinted with Permission from "Elastic and Plastic Characteristics of Sodium Metal" by Cole D. Fincher, Yuwei Zhang, George M. Pharr, and Matt Pharr, 2020. Applied Energy Materials, Volume 3, 1759-1767, Copyright 2020 by American Chemical Society.

3.1.2 Nanoindentation Methods

Nanoindentation measurements of hardness, *H*, and elastic modulus, *E*, were made using a Nanomechanics Nanoflip nanoindenter operated in the glove box with less than 0.1 ppm O_2 and H_2O (filled with argon gas from Praxair, 99.999% purity). All measurements were made with a Berkovich triangular pyramid indenter using the continuous stiffness measurement technique (CSM) at a frequency of 110 Hz with a target root-mean-square (RMS) amplitude of 1 nm[63, 104].

While precise knowledge of the indenter area function can typically be gathered from a fused silica calibration standard, the studies herein require measurements at much larger depths than can be easily achieved in fused silica. Thus, the fused silica area function was supplemented by measurements of data from polycarbonate (Makrolon®, 0.08 inch thickness, ASTM D3935 class 1 polycarbonate sheet) in a manner similar to that described by Ginder and Pharr[64]. This area function was calibrated over the range of 300 nm to 10 μm; as such, nanoindentation measurements outside of this range are not presented.

Indentation of Na requires considerations of indentation pile up due to its extremely high *E/H* ratio. Optical imaging of the contact area from nanoindentation tests (indented with target $\dot{P}/P = 0.05/\text{s}$) revealed that the contact depth was approximately 1.06 times the measured indenter penetration depth. Thus, in calculating the measured contact area A_c for this work, the reported contact depth was taken as 1.06 times the measured contact depth. We note that the degree of pile up should depend on the E/H ratio of a material, and thus the accuracy of the pile-up

assumption (that h_c/h = 1.06) should vary with depth for a material with depth-dependent hardness[62]. Additionally, a convenience afforded by Na's high *E/H* ratio is that very little elastic recovery occurs during unloading (the depth recovery is less than 1% of the total penetration depth). Thus, for hardness measurements, we can discard the typical sink-in correction to contact depth, rendering the hardness measurement independent of the measured contact stiffness. In all tests, the point of contact was initially identified based upon a 250 nm/s approach rate using a change of dP/dh of 100 N/m with data acquisition at 220 Hz. The point of contact was more accurately identified by visual inspection of the data after the test, with the estimation reflecting the point of contact to within 20 nm or better in depth.

3.1.4 Microhardness Testing

The same samples used for nanoindentation were also used for microhardness testing. After nanoindentation testing was complete, the sample and mount were submersed in mineral oil before removal from the glovebox to mitigate potential effects from air exposure. During transport, a glass slide was used to cover the surface of the sample while submerged in oil. Microhardness testing was conducted on the sample through 1 inch of oil using a Wilson TUKON 1102 Microhardness Tester with a Vickers tip. The loading to max force occurred over 5 seconds, followed by a prescribed dwell time at the maximum load. 20, 7, and 7 indents were conducted at maximum loads of 10, 25, and 50 gram-force, respectively, all with a 10 second dwell time at the maximum applied load. Subsequent optical imaging of the sample through oil and the glass slide enabled observation of the contact area of the microhardness indents, as well as validation of the ultimate contact area from nanoindentation. The presented microhardness results represent the

Meyer hardness, or the force divided by the projected area (as measured from optical microscopy). The corresponding microhardness indentation depth referenced within the results section was then estimated by approximating the indenter as having an ideal area function ($A_c = 24.5\ h_c^2$).

3.1.5 Bulk Compression Testing

For bulk tests, sodium cubes were cut within the glovebox into prisms with a rectangular cross sections possessing a width to height ratio of approximately 1.6 (width of 6 $\pm$ 1.2 mm, height of 10.5 $\pm$ 1.1 mm). After preparation, the cubes were measured with calipers and then stored under oil within the glovebox. Just before testing, the cubes were transferred to an oil bath and then removed from the glovebox (See Figure S10 for an example specimen). An Instron 5943 testing system was used to perform compression tests through the oil bath immediately upon removal from the glovebox. The samples were not observed to change color between removal from the glovebox and the conclusion of mechanical testing, thereby suggesting minimal effects of contamination.

3.1.6 Finite Element Analysis

Finite element analysis provided insight into the physical length scales probed by the nanoindentation measurements. The axisymmetric simulation presented in Figure 9 consisted of an analytical rigid surface (the indenter) possessing an internal angle of 70.2° (the cone angle with

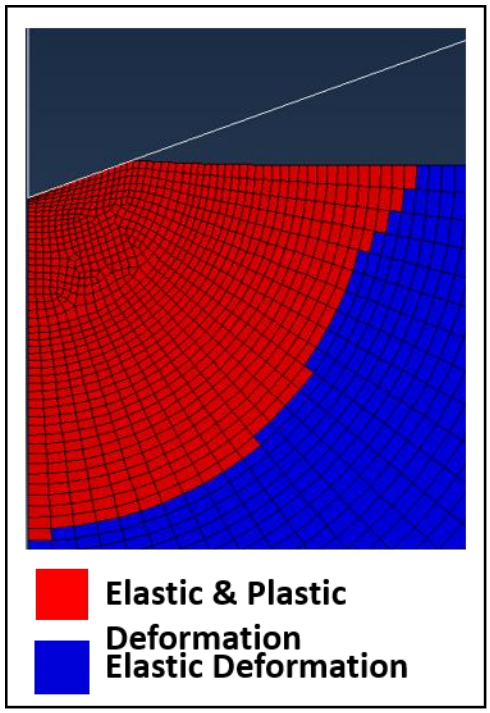

Figure 9. The actively yielding elements (AC_Yield output) from ABAQUS used to estimate the volume of the plastic zone under the indenter for nanoindentation experiments. The red region represents the elements undergoing plastic and elastic deformation, while the blue region undergoes elastic deformation only.

the same self-similar contact area with respect to depth as a Berkovich indenter tip) in contact with a solid mesh of 4 node axisymmetric elements (CAX4R) elements. Nonlinear geometric effects were included, and the elastic behavior of the solid was defined with an elastic modulus of 3.5 GPa and a Poisson's ratio of 0.3. The plastic flow stress was defined as a function of plastic strain by inputting the stress-strain data from an experimentally measured sodium compression stress-strain curve (for bulk compression to 30% strain at 0.1 %/s). The indenter in the simulation was specified to have x displacement, z displacement, and all rotations fixed at zero (U1 = U3 = UR2 = UR3 = UR1 = 0), with the indenter tip displaced downward into the solid (i.e., U2 = $-h_c$). The solid was defined as having a fixed boundary on the bottom-most surface with the left side

possessing a y-axis symmetric boundary condition. A finite-sliding interaction was defined between the indenter and solid surface, using surface-to-surface discretization and adjustment only to remove overclosure. This interaction was defined to have frictionless tangential behavior. For the input flow stresses, the simulations produced a plastic volume which (if treated as scaling like a hemisphere) possesses a radius of $11.1 * h_c$. Meanwhile, the von Mises stress decays to below 1% of the maximum value at a depth of $40.5 * h_c$.

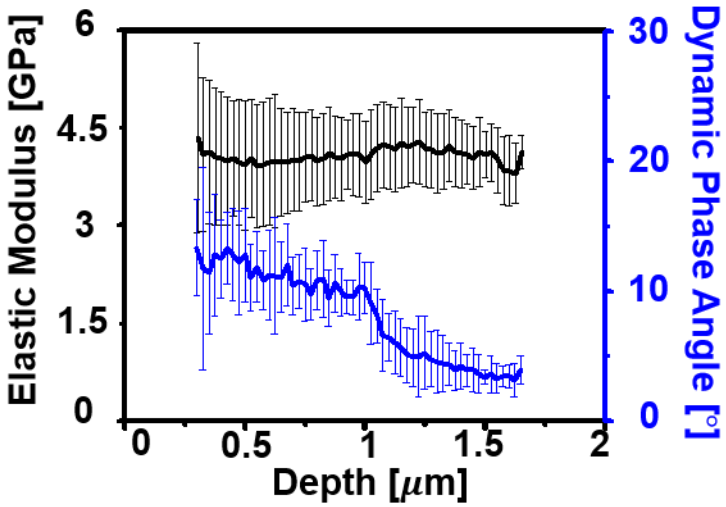

Figure 10. Elastic modulus and corresponding dynamic phase angle from 10 nanoindentation tests in Na. All tests were performed within 1 hour after surface preparation. The indents were conducted using a target loading rate divided by load of $\dot{P}/P$ = 0.05 [1/s] to a depth of 1 μm, followed by a 60 second constant load hold. Each color represents a different individual indent.

3.2 Results

3.2.1 Elastic Modulus

Figure 10 displays indentation measurements of Na conducted within one hour of sample preparation. Each curve represents the average of 10 tests, with the error bars spanning one standard deviation from the mean. These tests used a target $\frac{\dot{P}}{P} = 0.05/s$ loading scheme to a target depth of 1 μm, followed by a constant load hold for 60 seconds. Additional information regarding this test set, such as individual load-depth curves and the indentation strain rate, is provided in the supplementary information (Figure S12). As noted by Merle, in a material with a large E/H ratio, a high dynamic phase angle (e.g. 10 ° or higher) may reflect the encroachment of plastic deformation upon the dynamic displacement oscillation used for the continuous stiffness

measurement[105]. We note that the dynamic phase flattens out at a relatively small dynamic phase angle (near a few degrees) as the load hold begins at the 1 μm indentation depth, implying that plasticity error can be treated as negligible for depths larger than 1 μm. Because the elastic modulus does not appear to change significantly with depth, this sample does not seem to exhibit any effects of a surface film. As such, the elastic modulus observed during the load hold (3.9 ± 0.5 GPa) likely represents that of polycrystalline Na metal, i.e., the form typically used in battery applications.

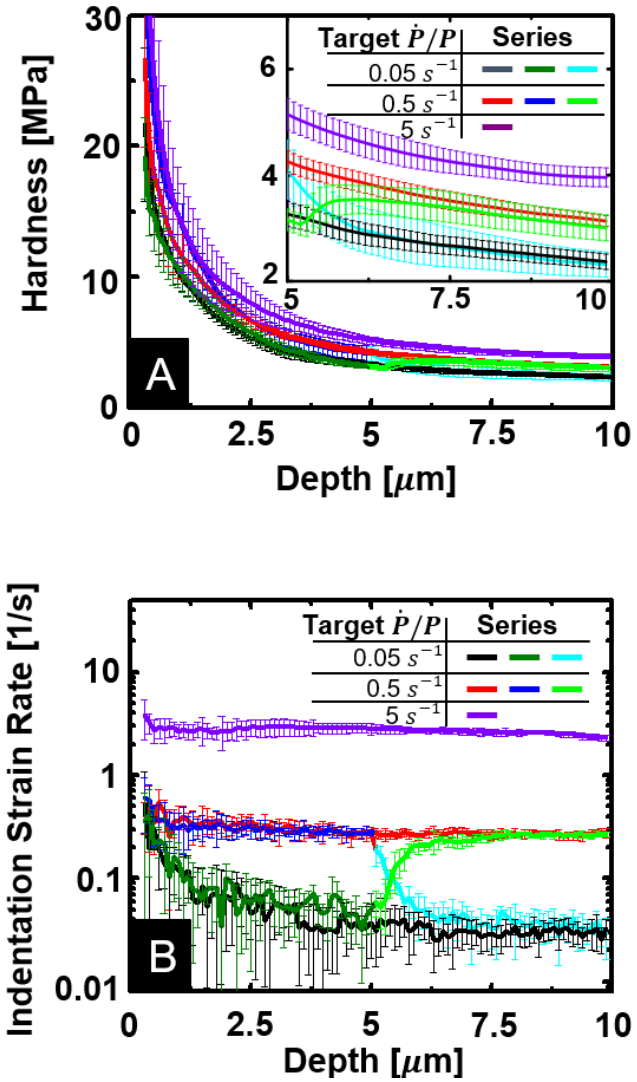

Figure 11. Nanoindentation tests, with each series representing the average of 7 or more individual indents conducted under identical test conditions. 11A) the indentation hardness, and 11B) the indentation strain rate (dimensionally, $\dot{h}/h$). Scatter bars span one standard deviation from the mean. All corresponding load-depth curves can be found in the supporting information.

3.2.2 Nanoindentation Hardness

Figure 11 shows the measured nanoindentation hardness of Na metal. Each curve represents the average of 7 tests. Individual indentation tests were placed randomly in the samples

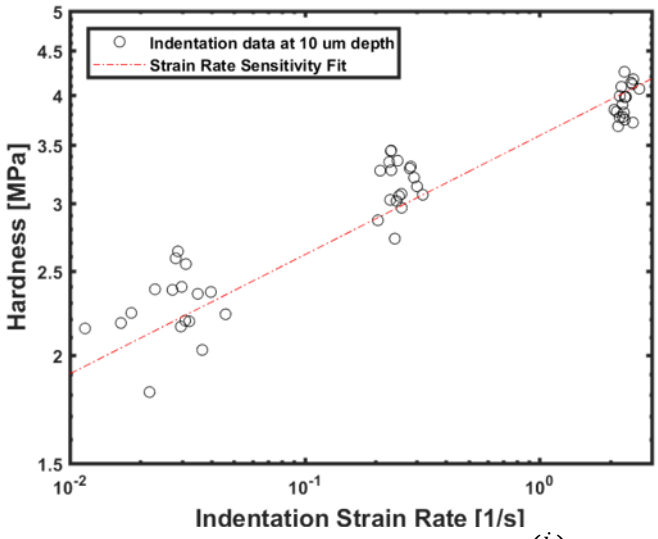

Figure 12. Indentation hardness versus indentation strain rate $\left(\frac{\dot{h}}{h}\right)$ measured at 10μm indentation depths for constant target $\frac{\dot{P}}{P}$ tests shown in Figure 3. The strain rate sensitivity fit follows the form of $H = \kappa \left(\frac{\dot{h}}{h}\right)^{m}$, where κ = 3.59 [MPa - s^m] and m = 0.138.

by moving > 2 mm between each indent. The error bars represent the standard deviations in the measured values at the corresponding depth. All data are plotted for depths of 0.3 μm (the lower bound for area function calibration) and larger. Plots of the loading rate by load versus depth, as well as the individual indentation load-depth curves, indentation strain rates versus depth, and hardness versus depth can be found in Figures S13-S18.

From Figure 11A, the hardness decreases significantly with depth before approaching a relatively constant value for the three tests conducted at a constant $\dot{P}/P$ (black, red and violet curves). While this decrease in hardness suggests an indentation size effect[106, 107], some variation may also arise from changes in strain rate (as seen in Figure 11B) during the test. Additionally, while no direct evidence of a surface film exists, its presence cannot completely be

ruled out. To determine whether history effects occurred, we implemented tests in which the target indentation strain rate was changed at a specified depth. Namely, in Figure 11A, the blue curve jumps from a target $\frac{\dot{P}}{P} = 0.5/s$ to $0.05/s$, while the green curve jumps from $\frac{\dot{P}}{P} = 0.05/s$ to $0.5/s$ at a depth of 5 μm. After brief transients following the jump, the indentation strain rates and hardnesses both recover to the hardnesses of the corresponding constant $\dot{P}/P$ tests, which indicates that Na's hardness is relatively history-independent under the tested conditions.

Because Na is relatively history independent and the strain rates approach a constant value, we attribute the difference in hardness among the three hardness at constant target $\frac{\dot{P}}{P}$ (black red, and violet curves) to rate dependent plasticity of Na metal. Fitting the indentation strain rate ($\dot{h}/h$) and hardness at a depth of 10 μm to the relationship $H = \kappa \left(\frac{\dot{h}}{h}\right)^m$ produces a strain-rate sensitivity exponent of m = 0.138, with a coefficient of $\kappa = 3.59\ [MPa - s^m]$, as seen in Figure 12.

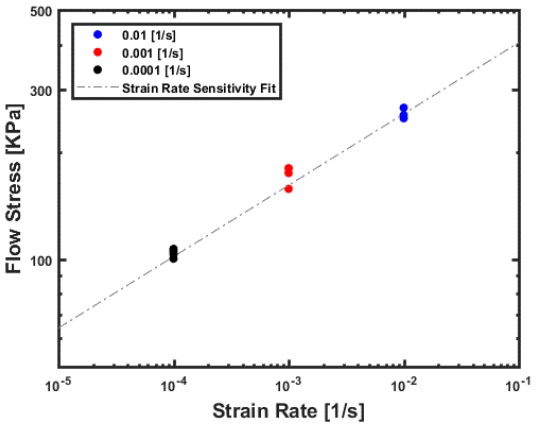

Figure 13. Strain rate versus the flow stress measured stress at 8% strain for bulk compression tests of sodium. The trend line represents the fit for strain rate sensitivity following $\sigma = \kappa * \dot{\epsilon}^m$, where κ = 0.64 [MPa - s^m] and m = 0.20

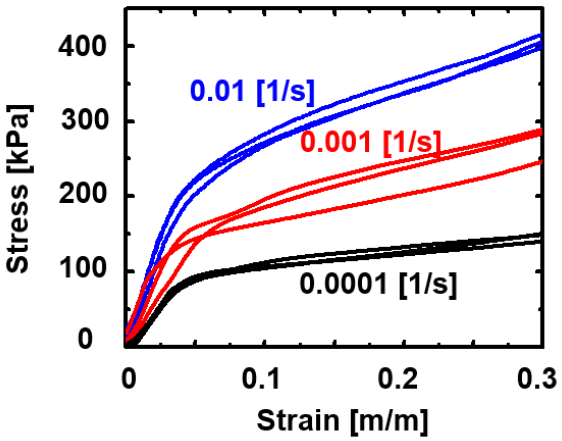

Figure 14. Stress-strain relationship for Na under bulk compression at several loading rates.

3.2.3 Bulk Compression

Figure 13 displays the engineering stress-strain response for compression testing of bulk sodium. The upper limit on the horizontal axis was chosen to omit data with testing artifacts associated with sample barreling at strains higher than 30% (as seen in Figure S19). While some fluctuations occur at low stress and strain values, perhaps due to slight misalignment between the sample surface and the compression platen, the stress-strain curves appear to be approximately linear at strains larger than 5% strain. At strains of 8%, the measured flow stresses were 102 $\pm$2.3 kPa, 170$\pm$12 kPa, and 254 $\pm$9.1 kPa at loading rates of 0.01%/s, 0.1%/s, and 1%/s, respectively, thereby indicating a significant rate dependence. Fitting the measured stress values at a specified strain (taken as $\epsilon = 0.08$) within this region to the relation $\sigma = \kappa * \dot{\epsilon}^m$ gives a strain rate sensitivity exponent of m = 0.20 with the coefficient $\kappa = 0.64\ [MPa - s^m]$, as seen in Figure 14.

3.2.4 Microhardness

Microhardness testing further attests to the soft nature of Na. Indents with loads at 10, 25, and 50 gram-force with a 10 second dwell time at the maximum load produced hardnesses of 1.6 $\pm$ 0.05 MPa, 1.2 $\pm$ 0.08 MPa, and 1.1 $\pm$ 0.09 MPa, respectively (mean $\pm$ standard deviation). Assuming that the indenter area function is ideal, the hardness measurements for the 10, 25, and 50 gram-force indents correspond to ultimate indentation depths of 50 $\pm$ 1, 91 $\pm$ 3, and 135 $\pm$ 5 μm, respectively. Indents conducted at 10 gram-force with a 60 second dwell time produced hardness measurements of 1.05 $\pm$ 0.06 MPa at ultimate depths of 60 $\pm$ 2 μm (as compared 1.6 $\pm$ 0.05 MPa measured using the same load but with a 10 second dwell time), thereby further attesting to the presence of rate-dependent plasticity.

3.2.5 Comparison with Lithium Metal

Figure 15A presents four indentation load-depth curves for both lithium and sodium, prepared and tested in identical fashions. The lithium data is taken from recent study of Fincher et

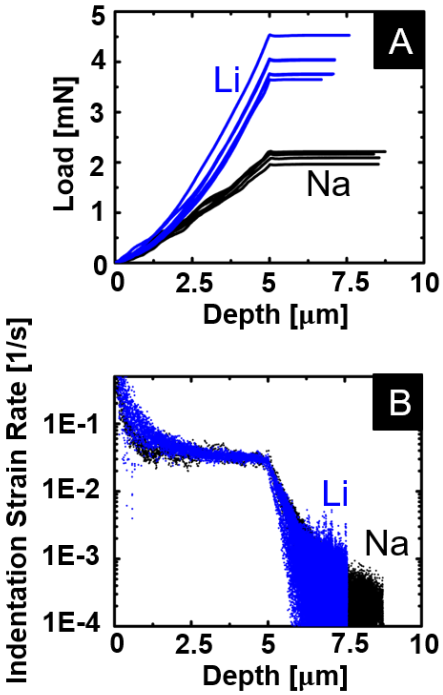

Figure 15A. Indentation load-depth curves on both lithium and sodium metal, and **15B.** the indentation strain rate ($\dot{\boldsymbol{h}}/\boldsymbol{h}$) versus depth, conducted at a target $\dot{\boldsymbol{P}}/\boldsymbol{P}$ = 0.05/s to a depth of 5 $\boldsymbol{\mu}$m, followed by a 30 minute load hold. The indenter tip drifts forward ~70% farther during the load hold for the sodium as compared to the lithium, despite the sodium hold occurring at a lower load.

al.[108]. For both materials, a target $\frac{\dot{P}}{P} = 0.05/s$ was used during the loading segment, up to a depth of 5 μm. Figure 15B shows that the indentation strain rates for both sets of experiments were similar during the loading period. Following the loading segment, the maximum load was held for a period of 30 minutes, allowing the indenter tip to creep deeper into the sample. On average, the indenter crept forward 3.6 μm during the load-hold for sodium indents, as compared to the 2.1 μm for the lithium indents. Overall, these tests indicate that Na is significantly softer and creeps significantly faster than Li.

3.3 Discussion

3.3.1 Elastic Properties of Sodium

A few previous studies have experimentally measured single crystal elastic constants of Na at varying temperatures using the ultrasonic pulse echo technique, as seen in the Table 1.

Reference Number	C11 (GPa)	C12 (GPa)	C44 (GPa)	Temp. (K)	E_{lower} (GPa)	E_{upper} (GPa)
[54]	5.34	2.31	2.04	200	4.59	4.60
[55]	7.39	6.22	4.19	299	4.56	6.08
[56]	8.21	6.83	5.77	78	5.62	7.92
	8.03	6.70	5.53	115	5.41	7.62
	7.83	6.53	5.27	155	5.25	7.32
	7.66	6.40	5.00	195	5.06	7.00
[57]	8.10	6.80	5.10	300	5.22	7.19
[58]	7.71	6.30	4.42	300	5.17	6.55

Table 1. Single Crystal Elastic Constants of Na Metal Measured through the Ultrasonic Pulse Echo Technique along with the Calculated Lower and Upper Bounds on the Elastic Modulus As Predicted by Hashin and Shtrikman.

E_{upper} and E_{lower} correspond to bounds on the aggregate elastic modulus as calculated by the Hashin and Shtrikman analysis using the corresponding single crystal elastic constants[109]. Our nanoindentation measurements of the elastic modulus (3.9 ± 0.5 GPa) are slightly lower than the predicted aggregate elastic modulus based on the application of the Hashin and Shtrikman model to the previous measurements in the above table. We argue that the most likely potential sources of experimental error have been eliminated: the area has been verified by optical

microscopy, while the phase angle data indicate that any "plasticity error" is minimal. One potential explanation for this discrepancy is that the sodium that we tested may possess some preferred crystal texture. This texture may affect the measured elastic modulus if the size of the elastically deformed zone is on the same order as the grain size. Still, despite being slightly smaller, our measured value of Na's modulus is similar in magnitude to Hashin and Shtrikman estimations based on measured single crystal elastic constants in literature.

When considering other candidate metallic anode materials for rechargeable batteries (e.g., Li and Mg which possess elastic moduli near 9.4 GPa[108] and 40 GPa[94], respectively as measured from similar nanoindentation), Na appears to possess a significantly lower elastic modulus (3.9 GPa) based on our nanoindentation results. The Newman and Monroe model, a popular model for describing the stability of the electrode-separator interface, predicts (using only linear elasticity) that implementing a separator with twice the shear modulus of the anode will prevent unstable and dendritic growth[9]. While this model does have significant limitations (e.g., not accounting for plastic deformation), it suggests that Na's low elastic modulus may assist in enhancing the stability of the separator-electrode interface (e.g., preventing metallic dendrite formation), at least under elastic loading.

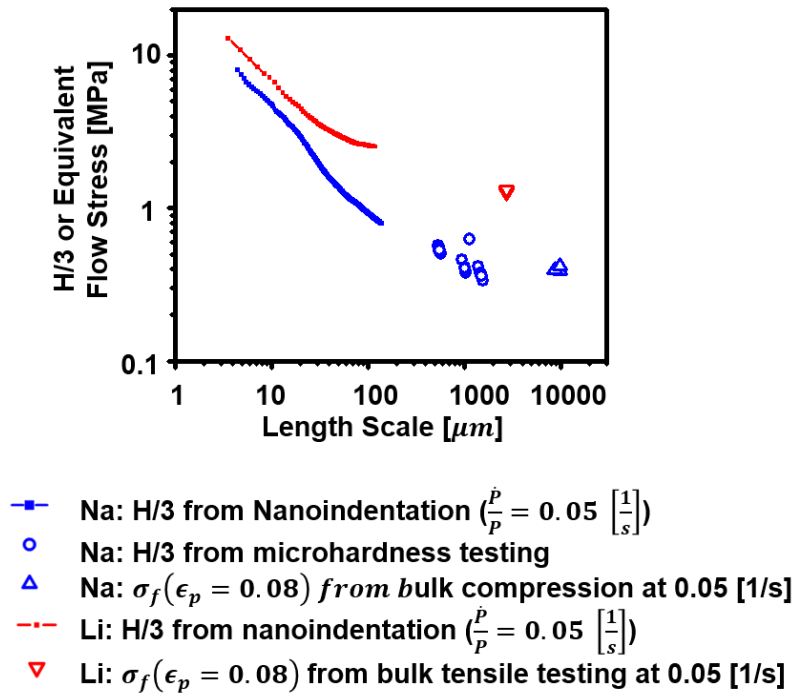

Figure 16. σ_f or H/3 is plotted versus representative length scale, displaying data from this study as well as the previous study of Fincher et al. on lithium metal.

3.3.2 Plastic Properties of Sodium

Figure 16 shows the measured equivalent flow stress of Na as a function of length scale for the bulk compression, microhardness, and nanoindentation tests provided in this study. In relating the nanoindentation and microhardness tests to an equivalent flow stress, we take the Tabor relation as $\sigma_f \cong H/3$. Previous studies of metals have shown that in this relation, the $H/3$ value from a Vickers or Berkovich tip geometry correlates with the flow stress at an equivalent strain of ≅8% from a uniaxial test[110]. Uniaxial compression curves for 0.05 [1/s] rate can be seen in Figure S9. We note that the presented Figure 16 does not account for the varied strain rates present in the different test methods (because there is no direct conversion from indentation strain rate to

bulk uniaxial compression strain rate, and thus the indentation strain rate and uniaxial strain rate are not strictly the same). However, we note that the nanoindentation measurements and the bulk compression experiments each show that the measured hardness or flow stresses vary by less than a factor of 3 at strains rates varying by over 2 orders of magnitude (as seen in Figures 11 and 13). Although significant, this variation is small compared to the variation in equivalent flow stress with length scale, as observed in Figure 16. Also, in constructing Figure 16, we argue that the length scale most appropriate for comparing the hardness among the various tests is the size of the plastic zone during the test. Thus, we use the equivalent plastic zone radius (11.1 times the indentation depth, as determined from finite element simulations – Figure 9) for the length scale associated with the nanoindentation and microhardness tests. For the bulk tests, we use the square root of the cross sectional area as the characteristic length.

The equivalent flow stress of Na from nanoindentation (from $\frac{\dot{P}}{P} = 0.05/s$) decreases from approximately 8 MPa to nearly 0.8 MPa as the characteristic length scale increases from 4.5 to 140 μm. The microhardness continues with a similar trend, decreasing from 560 to nearly 330 kPa as the length scale increases from 680 to 1950 μm. Finally, the bulk compression tests produce a flow stress of 190 kPa at a characteristic length scale near 10,000 μm.

3.3.3 Implications for Na batteries

Metallic lithium has been widely studied from an electrochemical perspective as a candidate anode material, owing to a number of excellent electrochemical characteristics; namely, it has the largest theoretical capacity of all anode materials. Figure 16 shows the data from Fincher et al.[108] for Li metal under equivalent testing conditions to the Na presented in this study. Comparing these two materials in terms of mechanical properties, Figure 16 indicates that Na is significantly softer than Li. In addition, Figure 15A indicates that Na creeps more readily than Li, as may be expected due to Na's lower melting point (~98°C for Na and 180°C for Li) and thus higher homologous temperature ($0.8T_m$ for Na and $0.65T_m$ for Li during the room temperature tests). Additionally, the bulk tests herein can be compared with previous studies of Li for further insight. The strain-rate sensitivity exponent of $m = 0.20$ (measured in this study) can be written as a stress exponent of $n = 5$ (for the equation $\dot{\epsilon} = A * \sigma^n$),, a value lower than the stress exponent measured for Li in various studies (n = 6.56[111], n = 6.6[112], and n = 6.55[108]). This comparatively low stress exponent from bulk tests only further indicates that Na is more prone to creep than Li.

These observations of sodium's soft nature have key implications in potential applications as metallic anodes. Due to Na being soft compared to Li, Na dendrites may have a greater propensity to blunt (i.e., flatten out) rather than puncture battery separators or solid electrolytes during solid-to-solid contact. Future experiments should seek to compare the mechanics of Li and Na metal during battery operation. Additionally, less externally applied pressure may be required to prevent the formation of Kirkendall voids (as compared to the pressures observed for formation in Li)[113]. Furthermore, fracture of the solid-electrolyte interphase (SEI) remains a significant

source of degradation and capacity fade of metallic batteries[114, 115]. Although relatively little is known regarding surface films on sodium, SEI layers tend to be relatively stiff. As such, sodium's soft nature likely leads to a large mismatch in mechanical properties at the SEI/electrode interface, which may have implications for electrode reversibility (e.g., through fracture, delamination or otherwise degrading the SEI layers)[36, 114, 115].

Additionally, the strain-rate sensitive response of Na has implications in practical battery systems. In a battery system, the charging rate maybe may be viewed as related to an applied strain rate, i.e., faster charging produces higher strain rates. Thus, the measured strain rate dependence of Na implies that dendrites may have larger strengths under faster charging rates. Furthermore, several studies of Li anodes suggest a relationship between charging rate and dendrite morphology, which may be at least partially attributable to strain-rate effects[116, 117]. While at least one recent study suggests that similar morphological transitions are present in Na[118], the importance of such rate-dependence in the Na system (and the influence of Na's rate-dependent plasticity) requires future study.

The observed size-dependence of hardness (Figure 11 and 16) also has implications in practical systems. In general, for defects at the SSE/anode interface, the size-dependence of Na's hardness may lead to stress relaxation or intensification depending on the defect size in a manner similar to that discussed by Herbert et al. in the context of Li[99]. Furthermore, dendrites initiate at small radii (likely at the nm scale), and grow to different sizes and shapes depending on the cell conditions[74, 78, 79, 119-121]. As such, the results in Figure 16 suggest that the mechanical properties of a Na electrodeposit will continuously evolve during nucleation and growth. These changes in mechanical properties during growth may influence the level of sustained stress in both

the electrodeposit and the surrounding solids as well as the subsequent morphological stability of the electrodeposit. For instance, if the electrodeposit becomes softer as it grows, a solid state electrolyte or stiff separator may be strong enough to prevent dendritic penetration (in a manner similar to the Newman and Monroe model as discussed above). Overall, the results in Figure 16 suggest a pronounced size effect of the plastic properties of sodium, which warrants future microstructural studies aimed at determining deformation mechanisms.

The formation and propagation of defects in SSE's remains a significant additional challenge for solid-state batteries. As potential disadvantage, Na's propensity for creep may lead to undesired deformation when subjected to static loads, e.g., so-called "stack pressure" in packaged batteries. To this end, the ability to readily flow/creep may facilitate transport of Na toward the cathode through grain boundaries in solid electrolytes, as has been observed in the Li system, which again warrant future studies[2, 122]. Furthermore, the enlarged size of the Na-ion as compared to the Li-ion (cation radius of 97 Å versus 68 Å, respectively[123]) may also result in more strain within the SSE during operation. At the same time, Na's low elastic modulus and relative softness may result in reduced stresses at the SSE/anode interface, reducing the propensity of SSE's to fracture.

For solid state batteries, interfacial contact (aka "interfacial wettability") between metallic anodes and the solid electrolyte remains a significant challenge. Some studies use a "press and pray" approach, introducing stack pressure and occasionally heat during assembly to establish "interfacial wettability[51, 124-126]." Still, loss of ionic contact may occur during cycling for a variety of reasons, e.g., the formation of ionically blocking layers due to side reactions, the loss of physical contact due to volume change of the electrode, or void formation due to stripping at the

interface[51, 126, 127]. However, the soft nature of Na may endow Na metal batteries with more conformal contact (as compared to Li and Mg) under pressure due to its facile deformation. Thus, Na's soft nature and propensity to creep may act as a boon towards establishing interfacial contact in solid-state batteries. In fact, recent studies from Bay et al.[128] and Wang et al.[129] demonstrate that the critical current densities for dendrite formation were approximately ten times higher for Na cycled across Na-Beta-alumina as compared to Li across garnet-type LLZO (despite both sets of experiments having a similar transference number). Bay et al.[128] attribute this comparatively high critical current density for the Na solid state battery to the "diffusive and mechanical properties of the alkali metal and solid-electrolyte." Furthermore, recent studies from Kasemchainan et al.[49] and Spencer Jolly et al.[50] indicate that creep plays the dominant role in maintaining interfacial contact in solid-state batteries. By comparing two recent studies, Kasemchainan[49] noted that Na metal could be cycled at higher current density than Li metal while maintaining interfacial contact, likely due to Na exhibiting greater creep[49, 50]. Towards this end, our study confirms that Na's creep is significantly more pronounced than Li. This finding only further indicates that Na metal should be capable of being cycled at higher current densities than Li metal while maintaining interfacial contact.

CHAPTER IV

SUMMARY[5,6]

4.1 Conclusions from Li metal

Nanoindentation and bulk tensile testing indicate that lithium metal exhibits significant strain rate sensitivity and size dependencies when tested at the nano to bulk-scales. The bulk yield stress of lithium varies from 0.57 to 1.26 MPa for strain rates from 5E-4 s^{-1} to 5E-1 s^{-1}. Tensile tests show that a steady state flow condition is reached at room temperature with a stress exponent of n = 6.55, which is comparable to a value of n = 6.9 as determined from constant $\dot{P}/P$ nanoindentation tests at 10 μm. The rate-sensitivity of lithium metal suggests that deformation mechanics may play a role in dictating the dendrite morphology, e.g., dendrite morphology depends significantly on current density, i.e., it depends on deposition/strain rate. Nanoindentation tests reveal that the hardness of lithium is not only rate dependent, but that the hardness exhibits significant size effects as well. For indentation tests conducted at constant target $\dot{P}/P$ = 0.05 s^{-1}, the nanoindentation hardness of lithium decreases from about 43 MPa at a depth of 250 nm to about 7.5 MPa (or an equivalent yield stress of 2.8 MPa using a constraint factor of 3) at a depth of 10 μm. Based on finite element analysis, the plastic zone underneath the nanoindentation extends to about 11 times the indentation depth. The length-scale dependency of Li's strength as measured in nanoindentation tests appears to diminish when the contact depth is on the order of

[5] Reprinted with Permission from "Mechanical properties of metallic lithium: from nano to bulk scales" by Cole D. Fincher, Daniela Ojeda, Yuwei Zhang, George M. Pharr, Matt Pharr, 2020. Acta Materialia, Volume 186, 215-222, Copyright 2019 by Acta Materialia Inc.

[6] Reprinted with Permission from "Elastic and Plastic Characteristics of Sodium Metal" by Cole D. Fincher, Yuwei Zhang, George M. Pharr, and Matt Pharr, 2020. Applied Energy Materials, Volume 3, 1759-1767, Copyright 2020 by American Chemical Society.

tens of microns. Li's size dependent properties may provide a means of tuning the deformation mechanics, and thus perhaps the robustness of the Li anode by adjusting the Li deposit sizes through design of 3D current collectors and seeding the deposition of Li, among other methods. As such, the results presented here may help to guide the design of battery architectures and charging conditions to mitigate unstable growth of Li during electrochemical cycling.

4.2 Conclusions from Na metal

In this thesis, we have quantified elastic and plastic properties of sodium metal at room temperature. Overall, this work shows that Na metal is extremely soft and compliant, readily creeps, and exhibits pronounced size effects. Specifically, nanoindentation revealed an elastic modulus of 3.9 ± 0.5 GPa, which is significantly smaller than other candidate metallic anodes, e.g., Li and Mg. Furthermore, we have shown that Na metal is both softer (indentation hardness less than 1/3 that of Li at indentation depth of 10 μm) and more prone to creep than Li metal. In addition, bulk, micro, and nanoscale testing reveal Na's marked size and strain-rate dependent plastic response. This strain-rate sensitivity suggests that mechanics may play a role in the deposition morphology: different morphologies may form at different deposition (i.e., strain) rates. Furthermore, the soft nature of Na metal may play a positive role in maintaining uniform deposit morphology and in maintaining anode-SSE contact. Towards this end, Na metal's relatively low flow stress and propensity to creep (compared to Li) should have significant implications for maintaining interfacial contact at high current densities. However, Na's extremely soft and creep-prone behavior may also exacerbate other failure modes (e.g., potentially leading to the transport of Na into SSE grain boundaries, which could precipitate fracture of the SSE). Overall, the results presented here provide general reference values for mechanical properties of Na metal and can

help guide the design of battery architectures and charging conditions towards reversible sodium metal batteries.

REFERENCES

1. Choi, N.S., et al., *Challenges facing lithium batteries and electrical double-layer capacitors.* Angewandte Chemie International Edition, 2012. **51**(40): p. 9994-10024.
2. Porz, L., et al., *Mechanism of lithium metal penetration through inorganic solid electrolytes.* Advanced Energy Materials, 2017. **7**(20): p. 1701003.
3. Tian, H.-K. and Y. Qi, *Simulation of the effect of contact area loss in all-solid-state Li-Ion batteries.* Journal of The Electrochemical Society, 2017. **164**(11): p. E3512-E3521.
4. Koerver, R., et al., *Chemo-mechanical expansion of lithium electrode materials–On the route to mechanically optimized all-solid-state batteries.* Energy and Environmental Science, 2018. **8**(11): p. 2142-2158.
5. Li, W.J., et al., *Fabrication and All Solid-State Battery Performance of TiS2 /Li10GeP2S12 Composite Electrodes.* Materials Transactions, 2016. **57**(4): p. 549-552.
6. Luntz, A.C., J. Voss, and K. Reuter, *Interfacial challenges in solid-state Li ion batteries.* J Phys Chem Lett, 2015. **6**(22): p. 4599-604.
7. Li, S., et al., *Developing High-Performance Lithium Metal Anode in Liquid Electrolytes: Challenges and Progress.* Adv Mater, 2018. **30**(17): p. 1706375.
8. Yurkiv, V., et al., *The influence of stress field on Li electrodeposition in Li-metal battery.* MRS Communications, 2018. **8**(03): p. 1285-1291.
9. Monroe, C. and J. Newman, *The impact of elastic deformation on deposition kinetics at lithium/polymer interfaces.* Journal of The Electrochemical Society, 2005. **152**(2): p. A396-A404.

10. Jana, A. and R.E. García, *Lithium dendrite growth mechanisms in liquid electrolytes.* J NanoEnergy, 2017. **41**: p. 552-565.

11. Gireaud, L., et al., *Lithium metal stripping/plating mechanisms studies: A metallurgical approach.* 2006. **8**(10): p. 1639-1649.

12. Wilkinson, D., et al., *Effects of physical constraints on Li cyclability.* Journal of power sources, 1991. **36**(4): p. 517-527.

13. Hirai, T., I. Yoshimatsu, and J.i. Yamaki, *Influence of electrolyte on lithium cycling efficiency with pressurized electrode stack.* Journal of The Electrochemical Society, 1994. **141**(3): p. 611-614.

14. Dollé, M., et al., *Live scanning electron microscope observations of dendritic growth in lithium/polymer cells.* Electrochemical solid-state letters, 2002. **5**(12): p. A286-A289.

15. Brissot, C., et al., *In situ study of dendritic growth inlithium/PEO-salt/lithium cells.* J Electrochemica Acts, 1998. **43**(10-11): p. 1569-1574.

16. Wood, K.N., M. Noked, and N.P. Dasgupta, *Lithium Metal Anodes: Toward an Improved Understanding of Coupled Morphological, Electrochemical, and Mechanical Behavior.* ACS Energy Letters, 2017. **2**(3): p. 664-672.

17. Krauskopf, T., et al., *Diffusion Limitation of Lithium Metal and Li–Mg Alloy Anodes on LLZO Type Solid Electrolytes as a Function of Temperature and Pressure.* Advanced Energy Materials, 2019: p. 1902568.

18. Sakamoto, J., *More pressure needed.* Nature Energy, 2019. **4**(10): p. 827-828.

19. Wang, M.J., R. Choudhury, and J. Sakamoto, *Characterizing the Li-Solid-Electrolyte Interface Dynamics as a Function of Stack Pressure and Current Density.* Joule, 2019. **3**(9): p. 2165-2178.

20. Mistry, A. and P. Mukherjee, *Molar Volume Mismatch: A Malefactor for Irregular Metallic Electrodeposition in Solid Electrolytes.* 2019.

21. Herbert, E.G., et al., *Nanoindentation of high-purity vapor deposited lithium films: A mechanistic rationalization of diffusion-mediated flow.* Journal of Materials Research, 2018. **33**(10): p. 1347-1360.

22. Xu, C., et al., *Enhanced strength and temperature dependence of mechanical properties of Li at small scales and its implications for Li metal anodes.* Proc Natl Acad Sci U S A, 2017. **114**(1): p. 57-61.

23. Schultz, R.P., *Lithium: Measurement of Young's Modulus and Yield Strength*. 2002, Fermi National Accelerator Lab., Batavia, IL (US).

24. Tariq, S., et al. *Li material testing-fermilab antiproton source lithium collection lens*. in *Particle Accelerator Conference, 2003. PAC 2003. Proceedings of the*. 2003. IEEE.

25. Masias, A., et al., *Elastic, plastic, and creep mechanical properties of lithium metal.* Journal of Materials Science, 2018. **54**(3): p. 2585-2600.

26. LePage, W.S., et al., *Lithium Mechanics: Roles of Strain Rate and Temperature and Implications for Lithium Metal Batteries.* Journal of The Electrochemical Society, 2019. **166**(2): p. A89-A97.

27. Campbell, C., et al., *Effect of nanopatterning on mechanical properties of Lithium anode.* Sci Rep, 2018. **8**(1): p. 2514.

28. Zheng, X., et al., *Sodium metal anodes for room-temperature sodium-ion batteries: Applications, challenges and solutions.* Energy Storage Materials, 2019. **16**: p. 6-23.

29. Anderson, D.L., *Chemical composition of the mantle.* Journal of Geophysical Research: Solid Earth, 1983. **88**(S01): p. B41-B52.

30. Jamesh, M.I. and A. Prakash, *Advancement of technology towards developing Na-ion batteries.* Journal of Power Sources, 2018. **378**: p. 268-300.

31. Kim, Y., et al., *High-Capacity Anode Materials for Sodium-Ion Batteries.* Chemistry–A European Journal, 2014. **20**(38): p. 11980-11992.

32. Eftekhari, A. and D.-W. Kim, *Sodium-ion batteries: new opportunities beyond energy storage by lithium.* Journal of Power Sources, 2018. **395**: p. 336-348.

33. Kim, H., et al., *Metallic anodes for next generation secondary batteries.* Chemical Society Reviews, 2013. **42**(23): p. 9011-9034.

34. Yui, Y., M. Hayashi, and J. Nakamura, *In situ microscopic observation of sodium deposition/dissolution on sodium electrode.* Scientific reports, 2016. **6**: p. 22406.

35. Adelhelm, P., et al., *From lithium to sodium: cell chemistry of room temperature sodium–air and sodium–sulfur batteries.* Beilstein journal of nanotechnology, 2015. **6**(1): p. 1016-1055.

36. Bieker, G., M. Winter, and P. Bieker, *Electrochemical in situ investigations of SEI and dendrite formation on the lithium metal anode.* Physical Chemistry Chemical Physics, 2015. **17**(14): p. 8670-8679.

37. Pfeifer, K., et al., *Can Metallic Sodium Electrodes Affect the Electrochemistry of Sodium-Ion Batteries? Reactivity Issues and Perspectives.* ChemSusChem, 2019: p. 3312-3319.

38. Hong, Y.-S., et al., *In operando observation of chemical and mechanical stability of Li and Na dendrites under quasi-zero electrochemical field.* Energy Storage Materials, 2018. **11**: p. 118-126.

39. Zhao, N., C. Li, and X. Guo, *Long-life Na–O 2 batteries with high energy efficiency enabled by electrochemically splitting NaO 2 at a low overpotential.* Physical Chemistry Chemical Physics, 2014. **16**(29): p. 15646-15652.

40. Gireaud, L., et al., *Lithium metal stripping/plating mechanisms studies: A metallurgical approach.* Electrochemistry communications, 2006. **8**(10): p. 1639-1649.

41. Liu, J., et al., *Pathways for practical high-energy long-cycling lithium metal batteries.* Nature Energy, 2019: p. 1.

42. Zhou, W., et al., *Rechargeable sodium all-solid-state battery.* ACS central science, 2017. **3**(1): p. 52-57.

43. Krauskopf, T., et al., *Toward a Fundamental Understanding of the Lithium Metal Anode in Solid-State Batteries—An Electrochemo-Mechanical Study on the Garnet-Type Solid Electrolyte Li6. 25Al0. 25La3Zr2O12.* ACS applied materials & interfaces, 2019. **11**(15): p. 14463-14477.

44. Cheng, L., et al., *The origin of high electrolyte–electrode interfacial resistances in lithium cells containing garnet type solid electrolytes.* Physical Chemistry Chemical Physics, 2014. **16**(34): p. 18294-18300.

45. Ferrese, A. and J. Newman, *Mechanical deformation of a lithium-metal anode due to a very stiff separator.* Journal of The Electrochemical Society, 2014. **161**(9): p. A1350-A1359.

46. Ferrese, A.J., *Electrochemical Modeling of a Lithium-Metal Anode*. 2013, UC Berkeley.

47. Pharr, M., et al., *Kinetics of initial lithiation of crystalline silicon electrodes of lithium-ion batteries.* Nano letters, 2012. **12**(9): p. 5039-5047.

48. Mistry, A. and P.P. Mukherjee, *Molar Volume Mismatch: A Malefactor for Irregular Metallic Electrodeposition in Solid Electrolytes.* ChemRxiv.org, 2019.

49. Kasemchainan, J., et al., *Critical stripping current leads to dendrite formation on plating in 3 lithium anode solid electrolyte cells.* Nature Materials, 2019.

50. Spencer Jolly, D., et al., *The sodium/Na beta" alumina interface: Effect of pressure on voids.* ACS Applied Materials & Interfaces, 2019.

51. Zhao, C., et al., *Solid-state sodium batteries.* Advanced Energy Materials, 2018. **8**(17): p. 1703012.

52. Kim, J.J., et al., *Progress in the Development of Sodium-Ion Solid Electrolytes.* Small Methods, 2017. **1**(10): p. 1700219.

53. Hou, W., et al., *Solid electrolytes and interfaces in all-solid-state sodium batteries: Progress and perspective.* Nano Energy, 2018.

54. Quimby, S. and S. Siegel, *The variation of the elastic constants of crystalline sodium with temperature between 80° K and 210° K.* Physical Review, 1938. **54**(4): p. 293.

55. Daniels, W.B., *Pressure variation of the elastic constants of sodium.* Physical Review, 1960. **119**(4): p. 1246.

56. Diederich, M.E. and J. Trivisonno, *Temperature dependence of the elastic constants of sodium.* Journal of Physics and Chemistry of Solids, 1966. **27**(4): p. 637-642.

57. Martinson, R., *Variation of the elastic constants of sodium with temperature and pressure.* Physical Review, 1969. **178**(3): p. 902.

58. Fritsch, G., F. Geipel, and A. Prasetyo, *The elastic constants of sodium from 20 to 95° C.* Journal of Physics and Chemistry of Solids, 1973. **34**(11): p. 1961-1969.

59. Edwards, C., *The Resistance of Metals to Penetration under Impact'.* Jl. Inst, of Metals, 1918: p. 61.

60. Herke, P.K., H. O. K; Schoeck, G. *Plastic Behaviour of Sodium*. in *4th International Conference on Strength of Metals and Alloys*.

61. Sargent, P. and M. Ashby, *Deformation mechanism maps for alkali metals.* Scripta metallurgica, 1984. **18**(2): p. 145-150.

62. Oliver, W.C. and G.M. Pharr, *Measurement of hardness and elastic modulus by instrumented indentation: Advances in understandings and refinements to methodology.* Journal of Materials Research, 2003. **19**(1): p. 3-20.

63. Oliver, W.C. and G.M. Pharr, *An improved technique for determining hardness and elastic modulus using load and displacement sensing indentation experiments.* Journal of Materials Research, 1992. **7**(6): p. 1564-1583.

64. Ginder, R.S., W.D. Nix, and G.M. Pharr, *A simple model for indentation creep.* Journal of the Mechanics and Physics of Solids, 2018. **112**: p. 552-562.

65. Hill, L.W., *Dynamic mechanical and tensile properties.* Paint coating testing manual, 1995. **14**: p. 534.

66. Kalidindi, S., A. Abusafieh, and E. El-Danaf, *Accurate characterization of machine compliance for simple compression testing.* Experimental Mechanics, 1997. **37**(2): p. 210-215.

67. Kassner, M.E., *Fundamentals of creep in metals and alloys*. 2015: Butterworth-Heinemann.

68. Gorgas, I., P. Herke, and G. Schoeck, *The plastic behaviour of lithium single crystals.* physica status solidi (a), 1981. **67**(2): p. 617-623.

69. Herbert, E.G., et al., *Nanoindentation of high-purity vapor deposited lithium films: A mechanistic rationalization of the transition from diffusion to dislocation-mediated flow.* Journal of Materials Research, 2018. **33**(10): p. 1361-1368.

70. Wang, Y. and Y.-T. Cheng, *A nanoindentation study of the viscoplastic behavior of pure lithium.* Scripta Materialia, 2017. **130**: p. 191-195.

71. Hull, D. and H.M. Rosenberg, *The Deformation of Lithium, Sodium, and Potassium at Low Temperatures: Tensile and Resistivity Experiments.* The Philosophical Magazine: A Journal of Theoretical Experimental and Applied Physics, 1959. **4**(39): p. 303-315.

72. Gibbs, J.W., et al., *The Three-Dimensional Morphology of Growing Dendrites.* Sci Rep, 2015. **5**: p. 11824.

73. Jana, A., D.R. Ely, and R.E. García, *Dendrite-separator interactions in lithium-based batteries.* Journal of Power Sources, 2015. **275**: p. 912-921.

74. Akolkar, R., *Mathematical model of the dendritic growth during lithium electrodeposition.* Journal of Power Sources, 2013. **232**: p. 23-28.

75. Barton, J. and J. Bockris, *The electrolytic growth of dendrites from ionic solutions.* Proc. R. Soc. Lond. A, 1962. **268**(1335): p. 485-505.

76. Diggle, J., A. Despic, and J. Bockris, *The mechanism of the dendritic electrocrystallization of zinc.* Journal of The Electrochemical Society, 1969. **116**(11): p. 1503-1514.

77. Oren, Y. and U. Landau, *Growth of zinc dendrites in acidic zinc chloride solutions.* Electrochemica Acta, 1982. **27**(6): p. 739-748.

78. Crowther, O. and A.C. West, *Effect of electrolyte composition on lithium dendrite growth.* Journal of The Electrochemical Society, 2008. **155**(11): p. A806-A811.

79. Cogswell, D.A., *Quantitative phase-field modeling of dendritic electrodeposition.* Physical Review E, 2015. **92**(1): p. 011301.

80. Love, C.T., *Perspective on the mechanical interaction between lithium dendrites and polymer separators at low temperature.* Journal of Electrochemical Energy Conversion and Storage, 2016. **13**(3): p. 031004.

81. Nishikawa, K., et al., *Li dendrite growth and Li+ ionic mass transfer phenomenon.* Journal of electroanalytical chemistry, 2011. **661**(1): p. 84-89.

82. Steiger, J., D. Kramer, and R. Mönig, *Mechanisms of dendritic growth investigated by in situ light microscopy during electrodeposition and dissolution of lithium.* Journal of Power Sources, 2014. **261**: p. 112-119.

83. Steiger, J., D. Kramer, and R. Mönig, *Microscopic observations of the formation, growth and shrinkage of lithium moss during electrodeposition and dissolution.* Electrochemica Acta, 2014. **136**: p. 529-536.

84. Li, Z., et al., *A review of lithium deposition in lithium-ion and lithium metal secondary batteries.* Journal of Power Sources, 2014. **254**: p. 168-182.

85. Wang, X., et al., *Stress-driven lithium dendrite growth mechanism and dendrite mitigation by electroplating on soft substrates.* Nature Energy, 2018. **3**(3): p. 227.

86. Bower, A.F. and P. Guduru, *A simple finite element model of diffusion, finite deformation, plasticity and fracture in lithium ion insertion electrode materials.* Modelling and Simulation in Materials Science and Engineering, 2012. **20**(4): p. 045004.

87. Xu, R. and K. Zhao, *Corrosive fracture of electrodes in Li-ion batteries.* Journal of the Mechanics and Physics of Solids, 2018. **121**: p. 258-280.

88. Chen, K.-H., et al., *Dead lithium: mass transport effects on voltage, capacity, and failure of lithium metal anodes.* Journal of Materials Chemistry A, 2017. **5**(23): p. 11671-11681.

89. Yoshimatsu, I., H. Toshiro, and J.-i. Yamaki, *Lithium Electrode Morphology during Cycling in Lithium Cells.* Journal of the Electrochemical Society, 1988. **135**(10): p. 2422-2427.

90. Lahiri, A. and F. Endres, *Review—Electrodeposition of Nanostructured Materials from Aqueous, Organic and Ionic Liquid Electrolytes for Li-Ion and Na-Ion Batteries: A Comparative Review.* Journal of The Electrochemical Society, 2017. **164**(9): p. D597-D612.

91. Cheng, X.B., et al., *Dendrite-Free Lithium Deposition Induced by Uniformly Distributed Lithium Ions for Efficient Lithium Metal Batteries.* Adv Mater, 2016. **28**(15): p. 2888-95.

92. Guan, X., et al., *Controlling Nucleation in Lithium Metal Anodes.* Small, 2018. **14**(37): p. e1801423.

93. Wang, Y., et al., *Mechanical behavior of electroplated mossy lithium at room temperature studied by flat punch indentation.* Applied Physics Letters, 2019. **115**(4): p. 043903.

94. Davidson, R., et al., *Formation of magnesium dendrites during electrodeposition.* ACS Energy Letters, 2018. **4**(2): p. 375-376.

95. Davidson, R., et al., *Mapping Mechanisms and Growth Regimes of Magnesium Electrodeposition at High Current Densities.* Materials Horizons, 2019.

96. Mehdi, B.L., et al., *The impact of Li grain size on coulombic efficiency in Li batteries.* Scientific reports, 2016. **6**: p. 34267.

97. Shi, F., et al., *Strong texturing of lithium metal in batteries.* Proceedings of the National Academy of Sciences, 2017. **114**(46): p. 12138-12143.

98. Watanabe, T., *Nano-plating: microstructure control theory of plated film and data base of plated film microstructure*. 2004: Elsevier.

99. Herbert, E.G., et al., *On the mechanisms of stress relaxation and intensification at the lithium/solid-state electrolyte interface.* Journal of Materials Research, 2019. **34**(21): p. 3593-3616.

100. Wang, L., et al., *Electrochemical corrosion behavior of nanocrystalline Co coatings explained by higher grain boundary density.* Electrochimica acta, 2007. **52**(13): p. 4342-4350.

101. Chandler, H., *Heat treater's guide: practices and procedures for nonferrous alloys*. 1996: ASM international.

102. Love, C.T., O.A. Baturina, and K.E. Swider-Lyons, *Observation of lithium dendrites at ambient temperature and below.* ECS Electrochemistry Letters, 2015. **4**(2): p. A24-A27.

103. Williams, D.B.G. and M. Lawton, *Drying of organic solvents: quantitative evaluation of the efficiency of several desiccants.* The Journal of organic chemistry, 2010. **75**(24): p. 8351-8354.

104. Pharr, G. and W. Oliver, *Measurement of thin film mechanical properties using nanoindentation.* Mrs Bulletin, 1992. **17**(7): p. 28-33.

105. Merle, B., V. Maier-Kiener, and G.M. Pharr, *Influence of modulus-to-hardness ratio and harmonic parameters on continuous stiffness measurement during nanoindentation.* Acta Materialia, 2017. **134**: p. 167-176.

106. Pharr, G.M., E.G. Herbert, and Y. Gao, *The indentation size effect: a critical examination of experimental observations and mechanistic interpretations.* Annual Review of Materials Research, 2010. **40**: p. 271-292.

107. Maier, V., et al., *Microstructure-dependent deformation behaviour of bcc-metals–indentation size effect and strain rate sensitivity.* Philosophical Magazine, 2015. **95**(16-18): p. 1766-1779.

108. Fincher, C.D., et al., *Mechanical Properties of Metallic Lithium: from Nano to Bulk Scales.* Acta Materialia, 2019.

109. Hashin, Z. and S. Shtrikman, *A variational approach to the theory of the elastic behaviour of polycrystals.* Journal of the Mechanics and Physics of Solids, 1962. **10**(4): p. 343-352.

110. Tabor, D., *The hardness of metals*. 2000: Oxford university press.

111. Masias, A., et al., *Elastic, plastic, and creep mechanical properties of lithium metal.* Journal of materials science, 2019. **54**(3): p. 2585-2600.

112. LePage, W.S., et al., *Lithium Mechanics: Roles of Strain Rate and Temperature and Implications for Lithium Metal Batteries.* Journal of The Electrochemical Society, 2019. **166**(2): p. A89-A97.

113. Lin, D., et al., *Fast galvanic lithium corrosion involving a Kirkendall-type mechanism.* Nature chemistry, 2019. **11**(4): p. 382.

114. Laresgoiti, I., et al., *Modeling mechanical degradation in lithium ion batteries during cycling: Solid electrolyte interphase fracture.* Journal of Power Sources, 2015. **300**: p. 112-122.

115. Lee, J.S., et al., *Metal–air batteries with high energy density: Li–air versus Zn–air.* Advanced Energy Materials, 2011. **1**(1): p. 34-50.

116. Brissot, C., et al., *In situ study of dendritic growth inlithium/PEO-salt/lithium cells.* Electrochimica acta, 1998. **43**(10-11): p. 1569-1574.

117. Dollé, M., et al., *Live scanning electron microscope observations of dendritic growth in lithium/polymer cells.* Electrochemical and solid-state letters, 2002. **5**(12): p. A286-A289.

118. Bayley, P.M., N.M. Trease, and C.P. Grey, *Insights into electrochemical sodium metal deposition as probed with in Situ 23Na NMR.* Journal of the American Chemical Society, 2016. **138**(6): p. 1955-1961.

119. Barton, J. and J.O.M. Bockris, *The electrolytic growth of dendrites from ionic solutions.* Proceedings of the Royal Society of London. Series A. Mathematical and Physical Sciences, 1962. **268**(1335): p. 485-505.

120. Diggle, J., A. Despic, and J.M. Bockris, *The mechanism of the dendritic electrocrystallization of zinc.* Journal of The Electrochemical Society, 1969. **116**(11): p. 1503-1514.

121. Oren, Y. and U. Landau, *Growth of zinc dendrites in acidic zinc chloride solutions.* Electrochimica Acta, 1982. **27**(6): p. 739-748.

122. Taylor, N.J., et al., *Demonstration of high current densities and extended cycling in the garnet Li7La3Zr2O12 solid electrolyte.* Journal of Power Sources, 2018. **396**: p. 314-318.

123. Pan, H., Y.-S. Hu, and L. Chen, *Room-temperature stationary sodium-ion batteries for large-scale electric energy storage.* Energy & Environmental Science, 2013. **6**(8): p. 2338-2360.

124. Hao, F., et al., *Architectural design and fabrication approaches for solid-state batteries.* MRS Bulletin, 2018. **43**(10): p. 775-781.

125. Cheng, E.J., A. Sharafi, and J. Sakamoto, *Intergranular Li metal propagation through polycrystalline Li6. 25Al0. 25La3Zr2O12 ceramic electrolyte.* Electrochimica Acta, 2017. **223**: p. 85-91.

126. Sakuda, A., A. Hayashi, and M. Tatsumisago, *Sulfide solid electrolyte with favorable mechanical property for all-solid-state lithium battery.* Scientific reports, 2013. **3**: p. 2261.

127. Manalastas Jr, W., et al., *Mechanical failure of garnet electrolytes during Li electrodeposition observed by in-operando microscopy.* Journal of Power Sources, 2019. **412**: p. 287-293.

128. Bay, M.C., et al., *Sodium Plating from Na-β "-Alumina Ceramics at Room Temperature, Paving the Way for Fast-Charging All-Solid-State Batteries.* Advanced Energy Materials, 2020. **10**(3): p. 1902899.

129. Wang, M., J.B. Wolfenstine, and J. Sakamoto, *Temperature dependent flux balance of the Li/Li7La3Zr2O12 interface.* Electrochimica Acta, 2019. **296**: p. 842-847.

130. Liu, Y.N., AHW., *Depth dependence of hardness in copper single crystals measured by nanoindentation.* Scripta Materialia, 2001. **44**(2): p. 237-241.

131. Herbert, E.G., et al., *Nanoindentation of high-purity vapor deposited lithium films: The elastic modulus.* Journal of Materials Research, 2018. **33**(10): p. 1335-1346.

APPENDIX A

SUPPORTING FIGURES

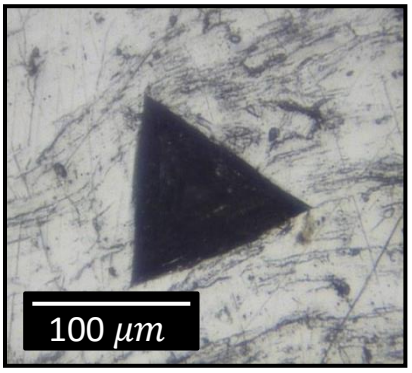

Figure S1. An indentation impression in lithium, imaged optically through a protective layer of oil and a glass slide.

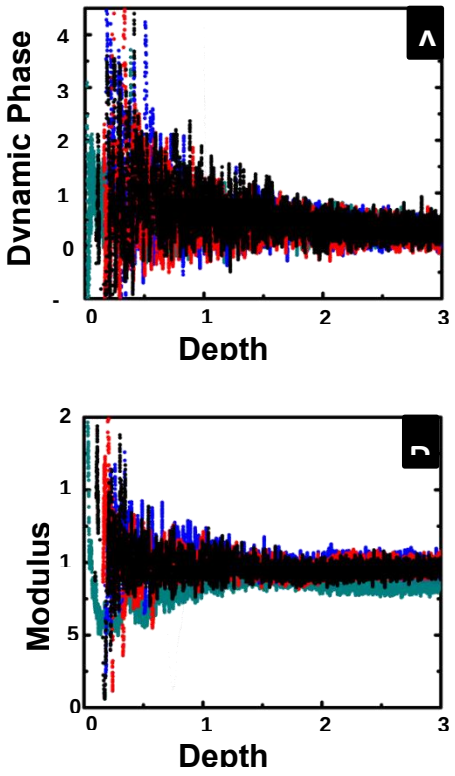

Figure S2. Nanoindentation tests conducted with a constant $\dot{P} = 12.5\frac{\mu N}{s}$ to a depth of 3 μm. A) the dynamic phase angle suggesting negligible plasticity error, B) the elastic modulus.

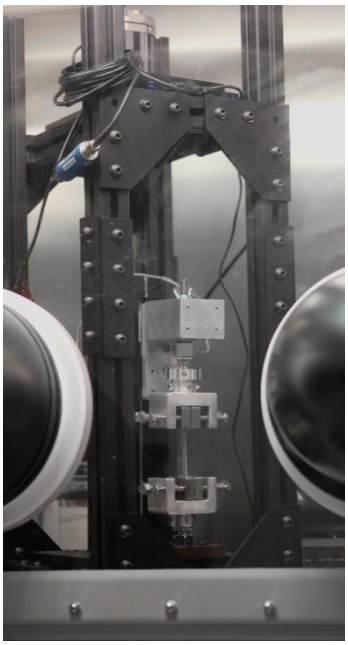

Figure S3. Photograph of the in-glovebox tensile tester.

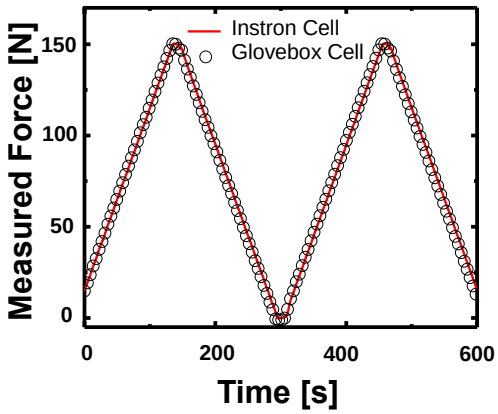

Figure S4. Force versus time verification test for the load cell used with in-glovebox tester, plotted against an Instron benchtop tensile tester model 5943 with a 1 kN load cell.

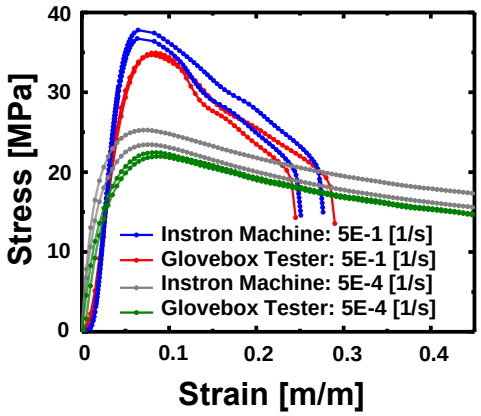

Figure S5. The stress-strain curves for high density polyethylene (HDPE) tensile testing samples from a standard Instron 5943 using a 1 kN load cell, and from our custom-built in-glovebox tensile tester. The HDPE specimens were acquired from Laboratory Devices Company, Cat. Number TPF012.

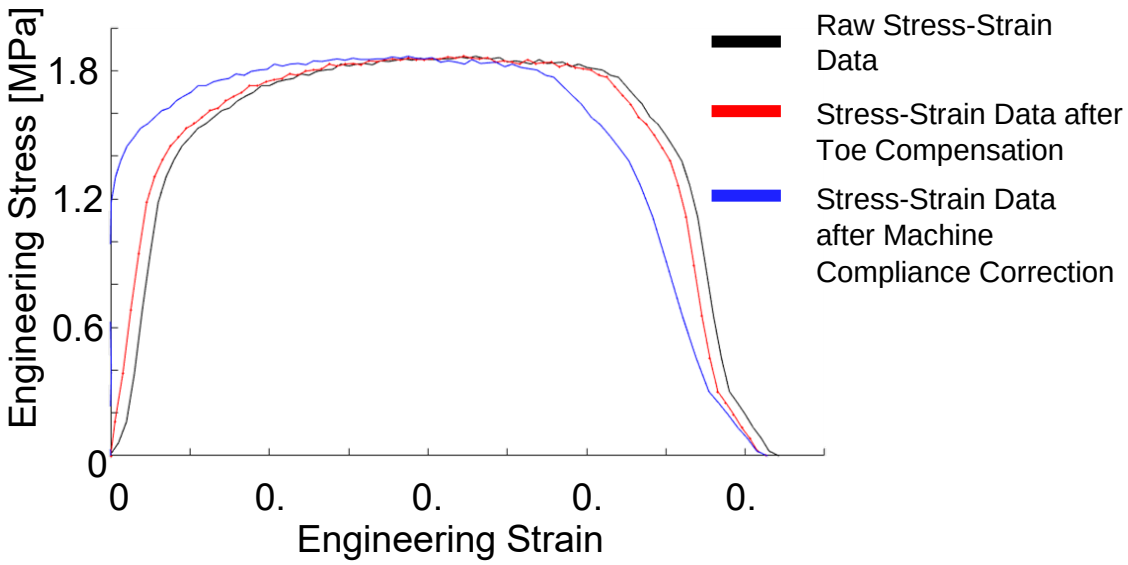

Figure S6. An example stress-strain curve displaying the effects of toe compensation and machine compliance correction.

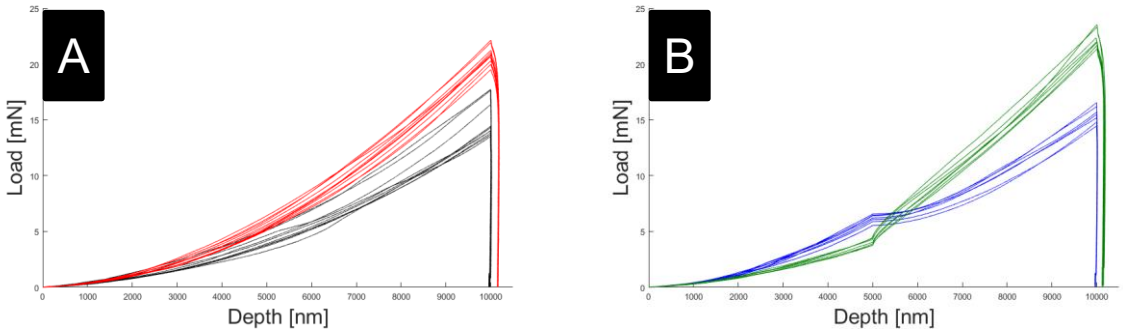

Figure S7. Load-Depth Curves for A) constant target P/P=0.05 [1/s] and P/P=0.5 [1/s] rate tests, and for B) Tests possessing a transition between target P/P values at 5 µm in depth. The unloading curves display a significant nose due to time-dependent plastic deformation (creep), especially for the data taken at high $\dot{P}/P$. As a result of this nose, the authors used continuous stiffness measurement for calculating stiffness rather than using the unloading curves.

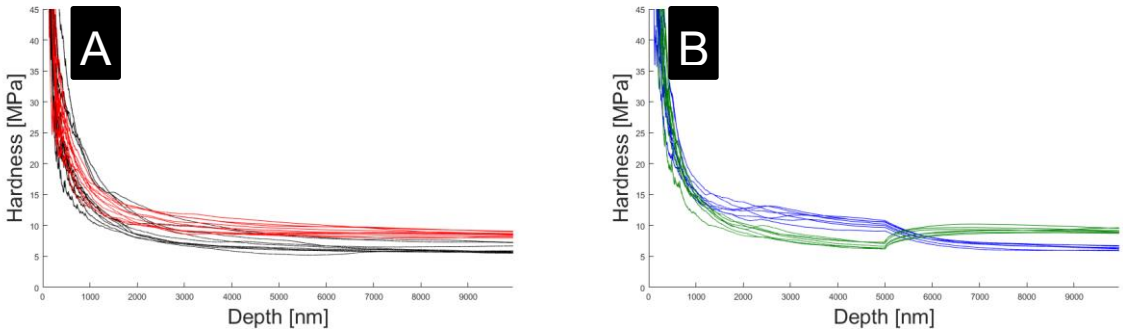

Figure S8. Hardness versus Depth measurements for A) constant target P/P=0.05 [1/s] and P/P=0.5 [1/s] rate tests, and for B) Tests possessing a transition between target P/P values at 5 µm in depth.

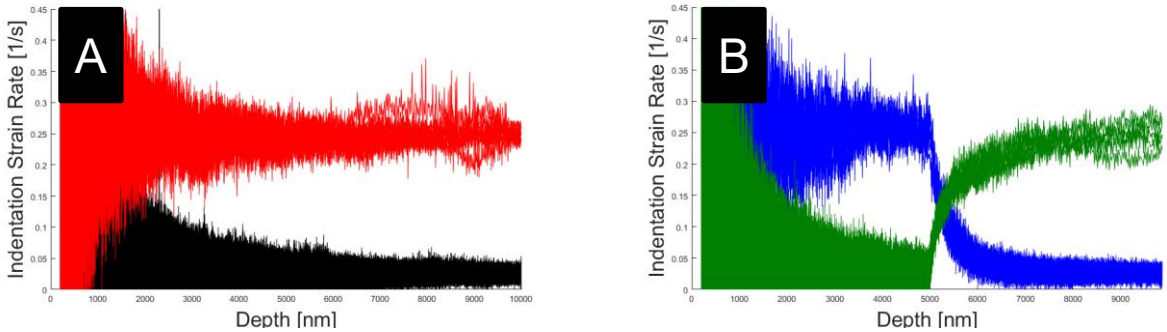

Figure S9. Indentation Strain Rate ($\dot{h}/h$) measurements versus Depth measurements for A) constant target P/P=0.05 [1/s] and P/P=0.5 [1/s] rate tests, and for B) Tests possessing a transition between target P/P values at 5 µm in depth.

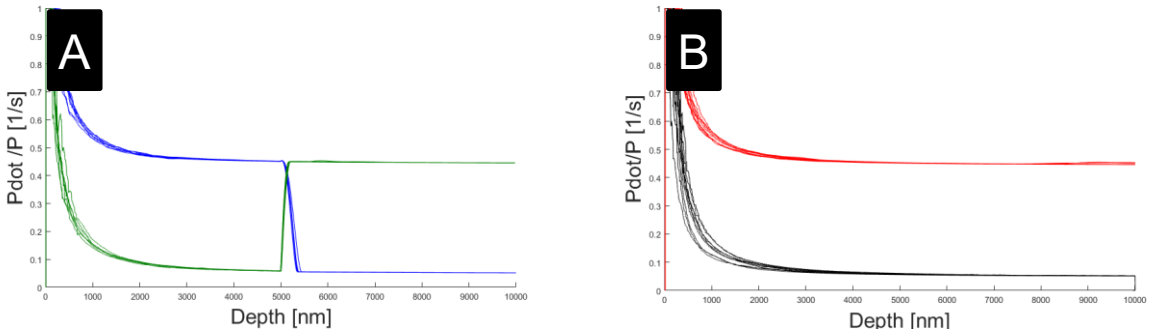

Figure S10. P/P versus Depth measurements for A) tests possessing a transition between target P/P values at 5 μm in depth and B) constant target P/P=0.05 [1/s] and P/P=0.5 [1/s] rate tests

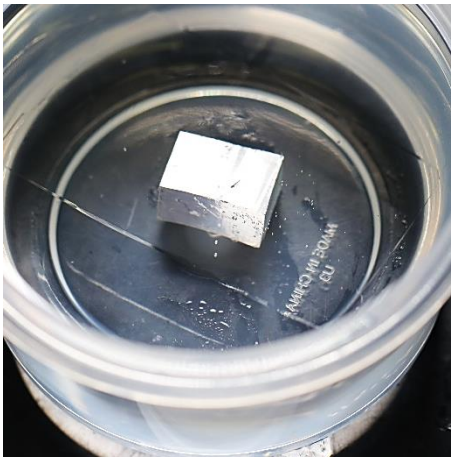

Figure S11. Picture of representative sodium specimen prepared for bulk compression test, stored under oil and a glass slide prior to testing.

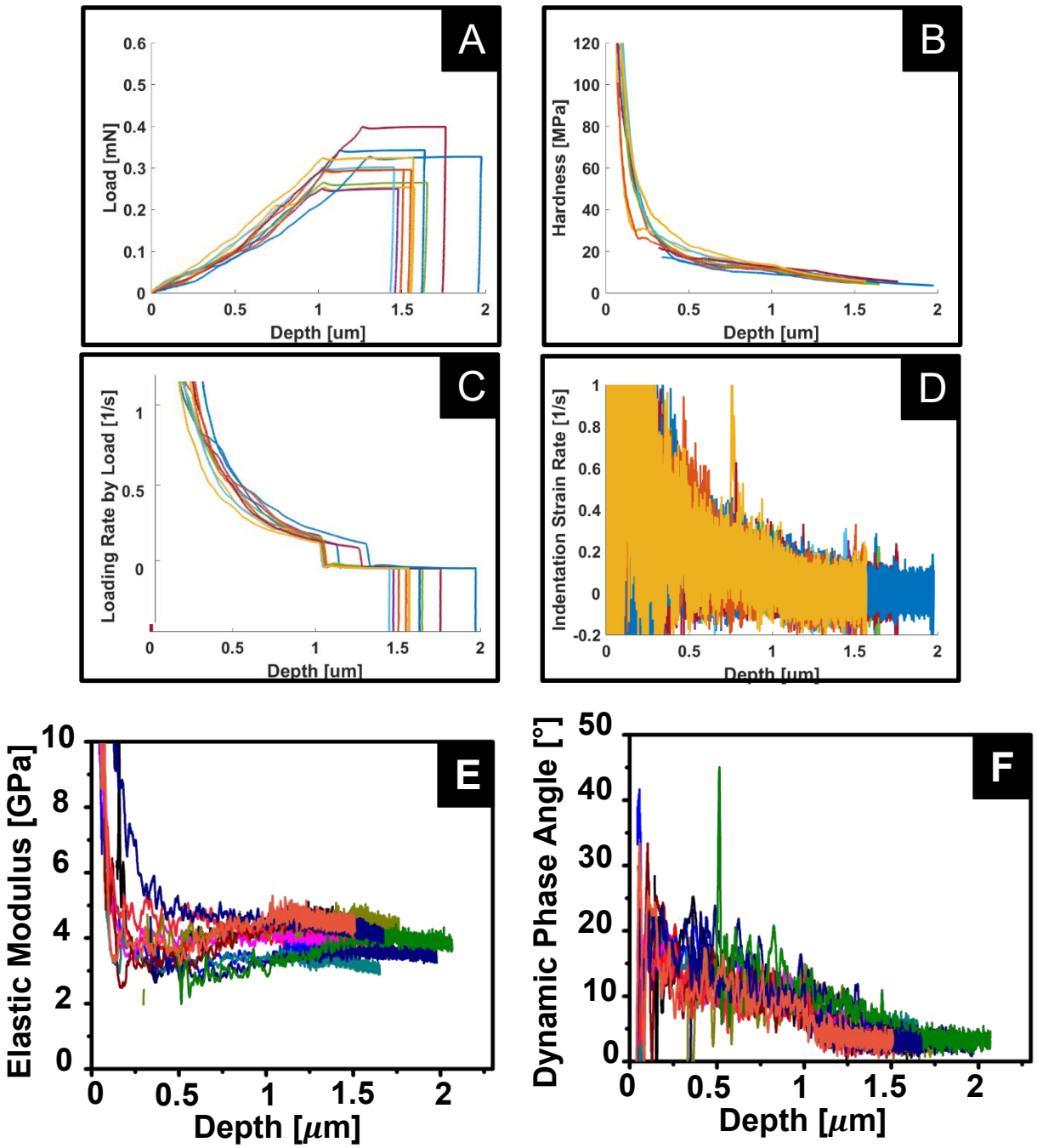

Figure S12. Individual curves for S12A) load-depth, S12B) indentation hardness, S12C) loading rate by load, S12D) indentation strain rate, S12E) elastic modulus, and S12F) dynamic phase angle corresponding to tests presented in Figure 1. Indents were conducted within 1 hour after sample preparation by using a target loading rate divided by load of $\dot{P}/P$ = 0.05 [1/s] to a depth of 1 μm, followed by a 60 second constant load hold. Due to imperfect surface recognition, some tests deviate slightly in the depth at which the load hold begins.

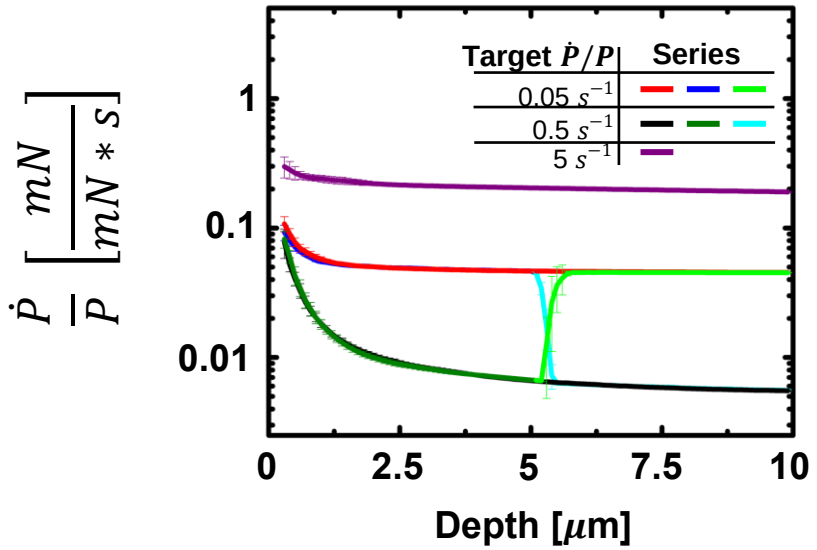

Figure S13. Loading rate by load versus depth corresponding to indentation data presented in Figure 11.

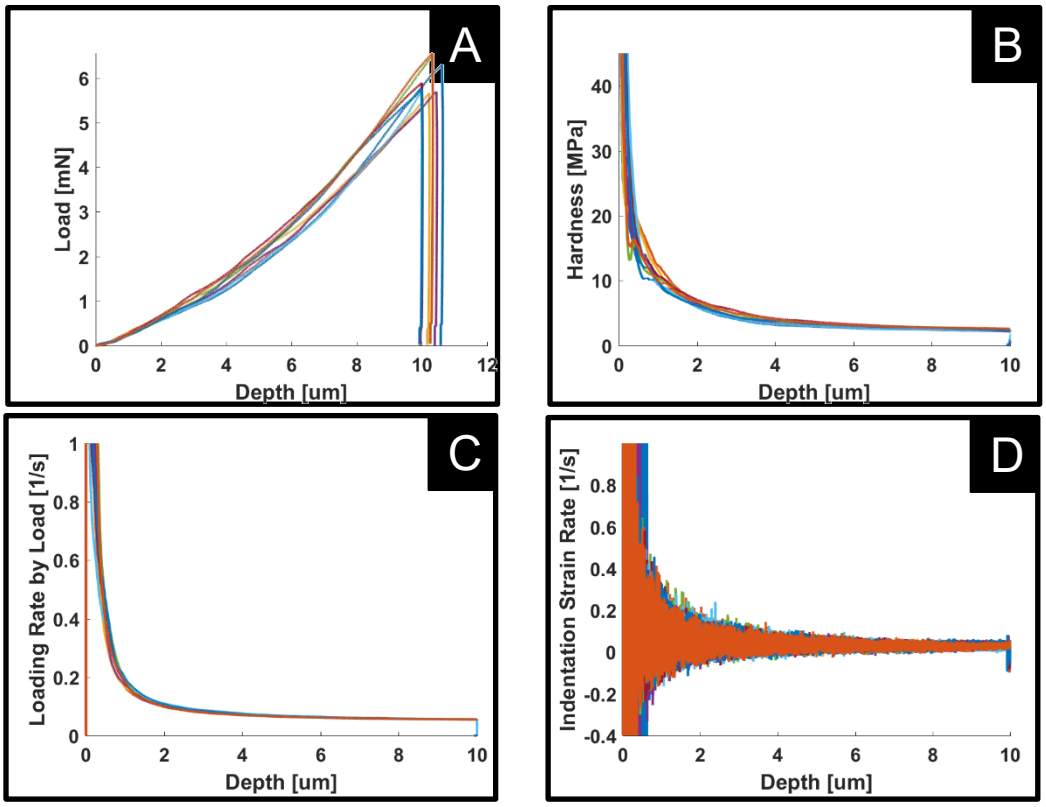

Figure S14. Individual curves for S14A) load versus depth, S14B) hardness versus depth, S14C) loading rate by load versus depth, and S14D) indentation strain rate data corresponding to the data presented in Figure 11 for indents conducted within three hours of sample preparation, using a target loading rate divided by load of $\dot{P}/P$ = 0.05 [1/s] to a depth of 10 μm.

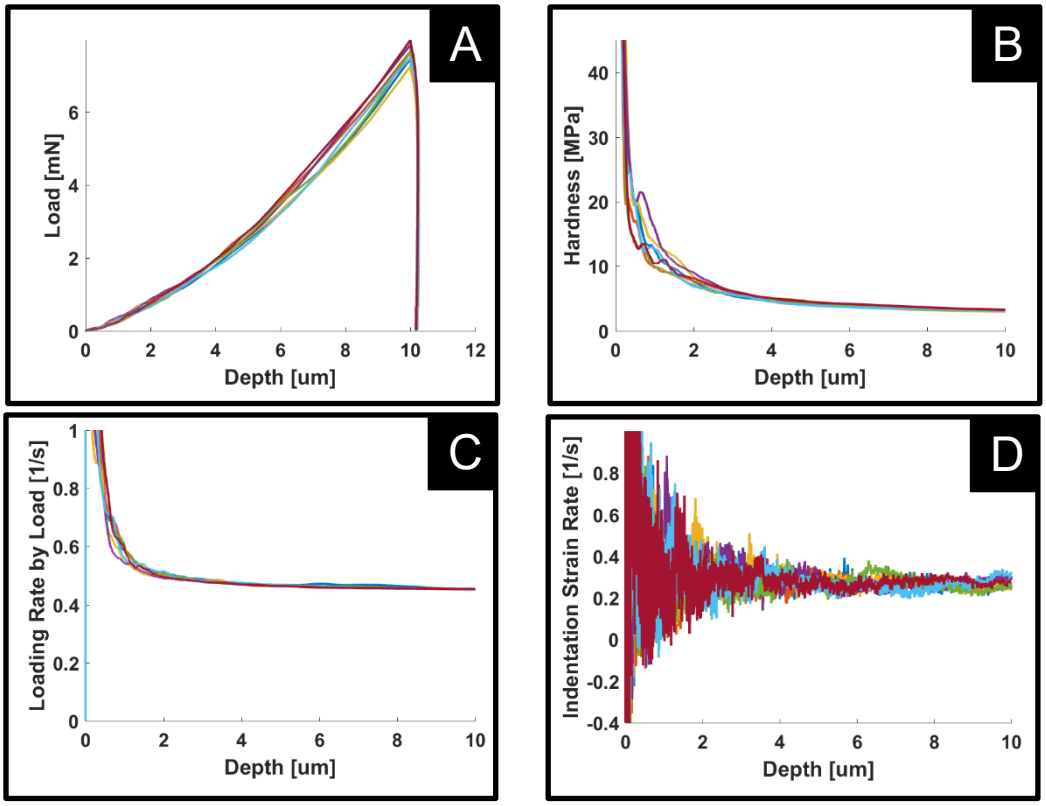

Figure S15. Individual curves for S15A) load versus depth, S15B) hardness versus depth, S15C) loading rate by load versus depth, and S15D) indentation strain rate data corresponding to the data presented in Figure 3 for indents conducted within three hours of sample preparation, using a target loading rate divided by load of $\dot{P}/P$ = 0.5 [1/s] to a depth of 10 μm.

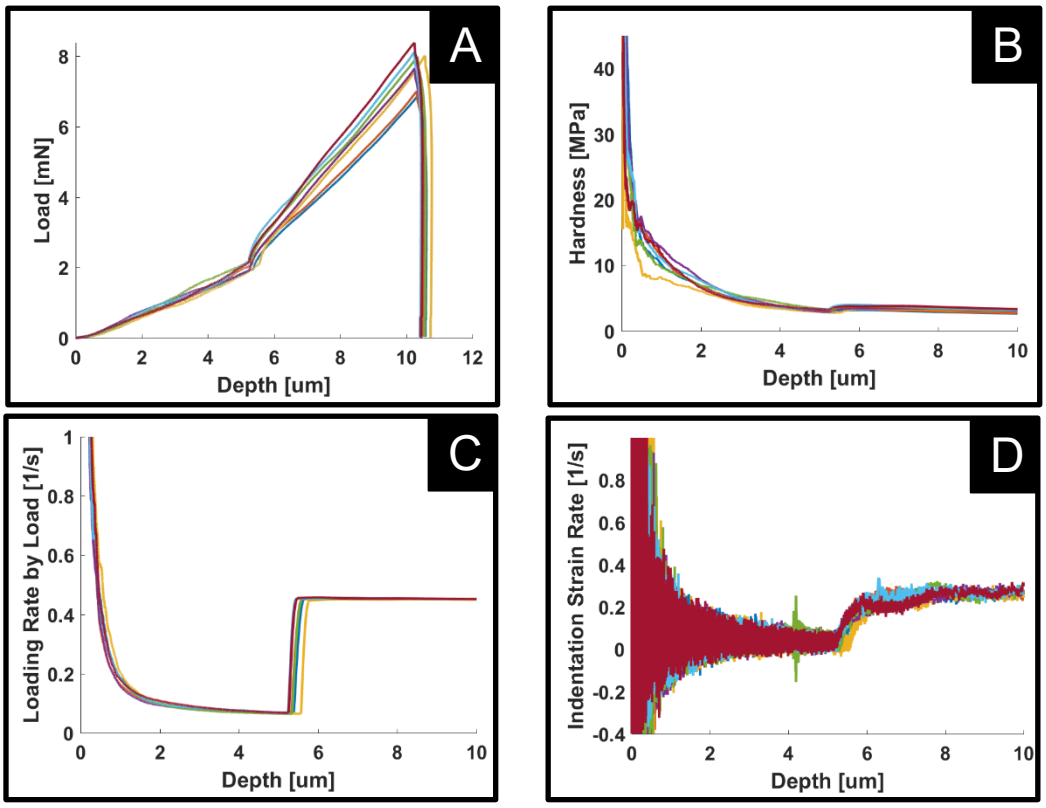

Figure S16. Individual curves for S16A) load versus depth, S16B) hardness versus depth, S16C) loading rate by load versus depth, and S16D) indentation strain rate data corresponding to the data presented in Figure 11 for indents conducted within three hours of sample preparation, using a target loading rate divided by load of $\dot{P}/P$ = 0.05 [1/s] to a depth of 5 μm followed by a jump to $\dot{P}/P$ = 0.5 [1/s] from depths 5 μm to 10 μm.

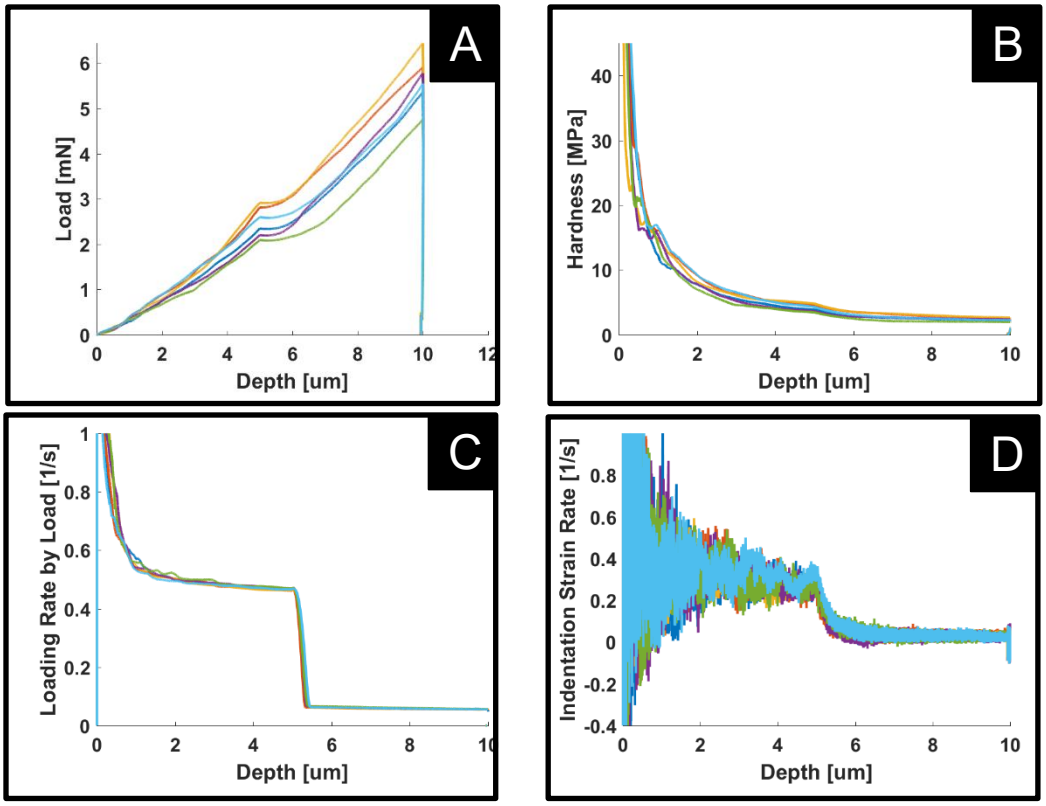

Figure S17. Individual curves for S17A) load versus depth, S17B) hardness versus depth, S17C) loading rate by load versus depth, and S17D) indentation strain rate data corresponding to the data presented in Figure 11 for indents conducted within three hours of sample preparation, using a target loading rate divided by load of $\dot{P}/P$ = 0.5 [1/s] to a depth of 5 μm followed by a jump to $\dot{P}/P$ = 0.05 [1/s] from depths 5 μm to 10 μm.

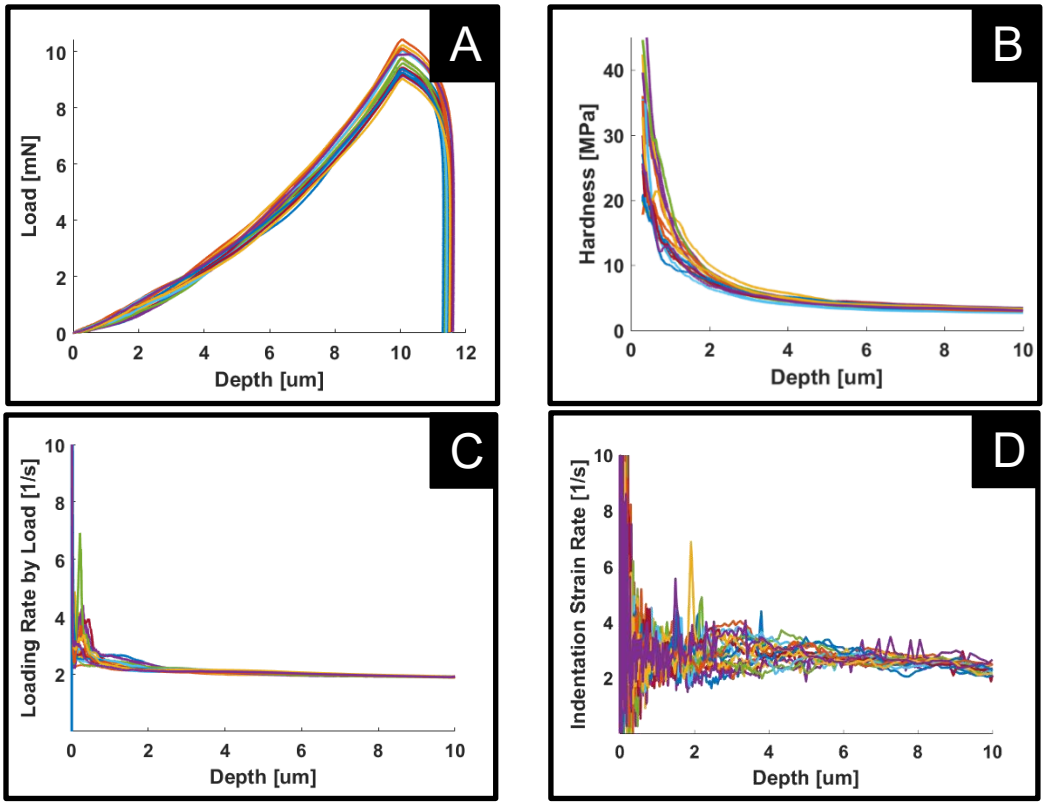

Figure S18. Individual curves for S18A) load versus depth, S18B) hardness versus depth, S18C) loading rate by load versus depth, and S18D) indentation strain rate data corresponding to the data presented in Figure 11 for indents conducted within three hours of sample preparation, using a target loading rate divided by load of $\dot{P}/P = 5$ [1/s] to a depth of 10 μm.

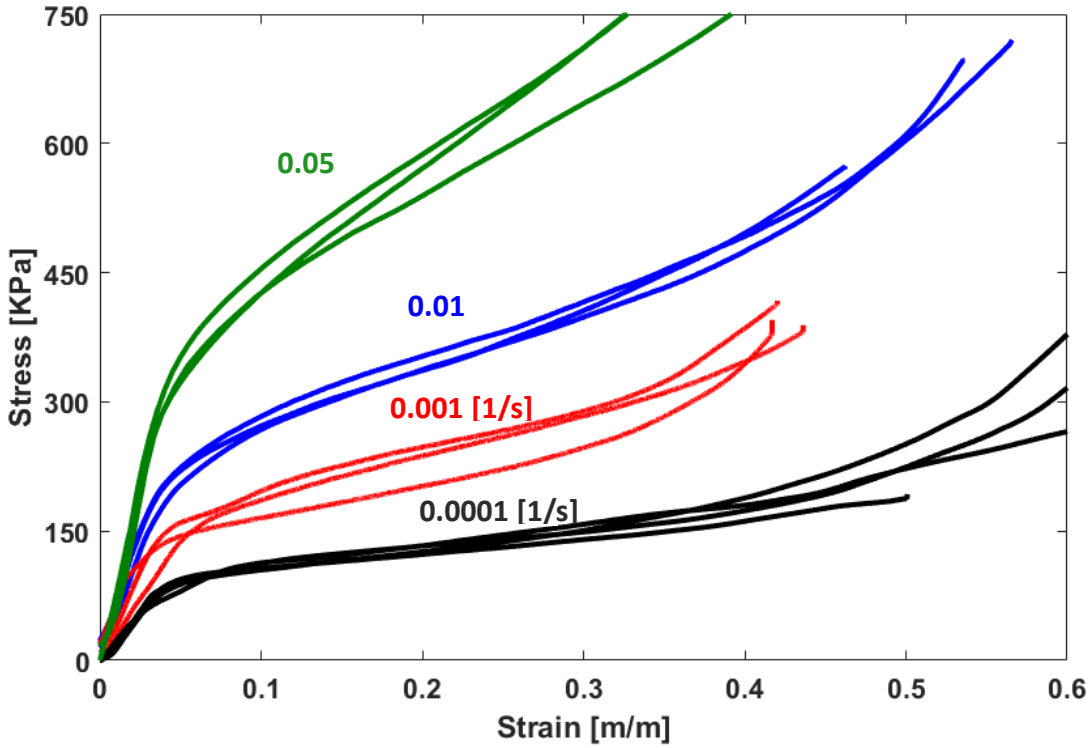

Figure S19. Full range of stress-strain curves, where significant experimental artifacts (i.e., sample barreling) can be seen to affect the stress-strain response at strains significantly larger than 0.3 [m/m].

APPENDIX B

ASSESSING THE POSSIBILITY OF SURFACE DAMAGE DURING SAMPLE PREPARATION

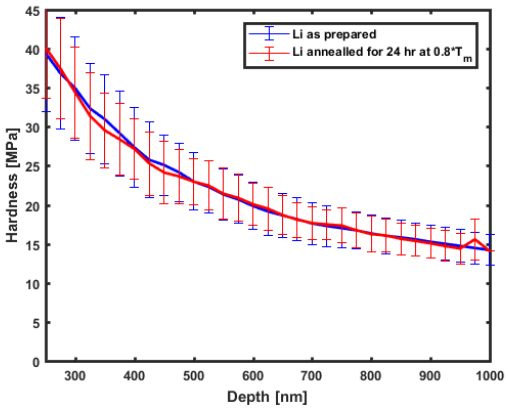

Figure B-1) Hardness measurements taken at a constant loading rate of 5 μN/s for Li as-prepared and after annealing for 24 hours at 0.8*T_m. Each series represents the average of seven indentation tests, with the error bars representing the standard deviation.

As is commonly known in literature, surface damage during preparation can significantly affect the degree of the indentation size effect[106, 130]. Thus, care must be taken to assess whether the indentation size effect found in this study is merely an artifact of sample preparation. Annealing is a common technique for removing effects of processing (coldworking) in a metal. Specifically, recrystallization commonly takes place at a temperature between 0.2 and 0.6 times the melting temperature T_m [101](T_m = 180.5°C for Li). Given that Li is already at 0.6*T_m at room temperature, some degree of annealing likely takes place naturally. Indeed, Herbert et al.[131] did observe grain boundary grooving and growth during storage, indicating that significant damage relief likely does occur even at room temperature. Still, we conducted

additional tests to assess whether the sample preparation used in this paper resulted in measurable changes in mechanical properties. A sample of lithium was prepared as per the discussed procedure in the methods section. This sample was then indented under constant loading rate conditions ($\dot{P} = 5\ \mu N/s$) to a depth of 1 μm. The indents were placed randomly around the sample, more than several mm apart. The sample was then placed on a hot plate at 100°C ($\approx 0.8 * T_m$) for 24 hours. After this time, the sample was then indented again (at room temperature) using the same procedures. Figure B-1 displays the hardness as a function of depth for both the Li sample as prepared, as well as after annealing. Each line represents the average of seven individual indentation tests. Figure B-2A and B-2B show the individual hardness versus depth curves and load versus depth curves. The trend lines in Figure B-1 appear extremely similar, indicating that the hardness is likely very similar before and after annealing. Given the high temperature of this annealing relative to the melting temperature, any changes in microstructure induced by the sample preparation process is likely removed. Thus, the minimal observed change in hardness implies that very little change in microstructure occurred during the annealing. Minimal changes in the material during annealing could indicate one of two points: 1) that the sample preparation imparted very little change (damage) to the sample in the first place, or 2) that any change imparted by sample preparation was rapidly annealed out prior to the

taking of any indentation measurements.

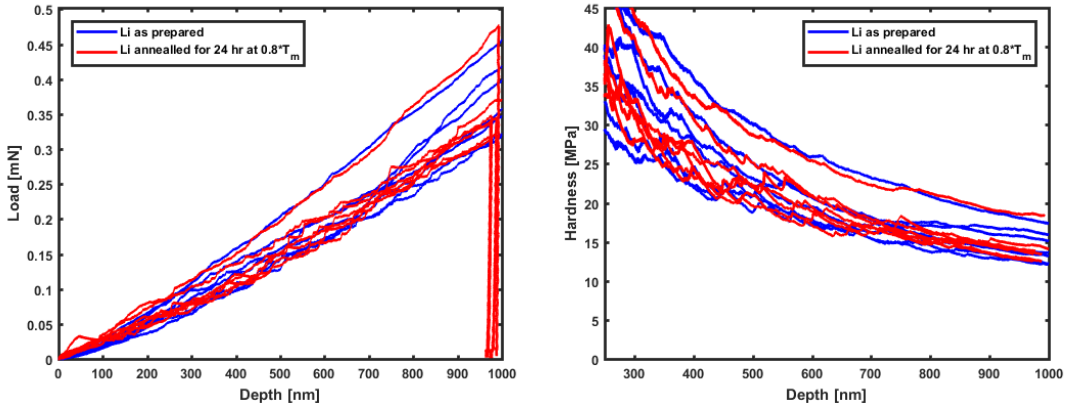

Figure B-2A) Load depth curves for Li metal indented at 5 μN/s, with blue curves representing the Li metal as prepared for this study and red curves representing Li metal after annealing for 24 hours at 0.8*T_m. **B-2B)** Hardness versus depth curves for Li metal indented at 5 μN/s, with blue curves representing the Li metal as prepared for this study and red curves representing Li metal after annealing for 24 hours at 0.8*T_m.